The tumor–normal interface shapes spatial immune programs in colorectal cancer

Aki Uesugi[1,2], Jongwoo Kim[2,3], Joe Yeong[4,5,6,7], Su Bin Lim[1,2*], Dakeun Lee[2,3*]

[1] Department of Biochemistry & Molecular Biology, Ajou University School of Medicine, Suwon, South Korea

[2] BK21 R&E Initiative for Advanced Precision Medicine, Department of Biomedical Sciences, Graduate School of Ajou University, Suwon, South Korea

[3] Department of Pathology, Ajou University School of Medicine, Suwon, South Korea

[4] Institute of Molecular and Cell Biology (IMCB), Agency for Science Technology and Research (A*STAR), Singapore, Singapore

[5] Department of Anatomical Pathology, Singapore General Hospital, Singapore, Singapore

[6] Singapore Immunology Network (SIgN), Agency for Science Technology and Research (A*STAR), Singapore, Singapore

[7] Cancer Science Institute, National University of Singapore, Singapore, Singapore

*** To whom correspondence should be addressed.**

Su Bin Lim, Department of Biochemistry & Molecular Biology, Ajou University School of Medicine, Suwon 16499, South Korea. Tel.: +82-31-219-5056; E-mail: sblim@ajou.ac.kr

Dakeun Lee, Department of Pathology, Ajou University School of Medicine, Suwon 16499, South Korea. Tel.: +82-31-219-7054; E-mail: dakeun@ajou.ac.kr

Abstract

Rationale

The tumor–normal interface represents a unique spatial compartment where colorectal cancer (CRC) directly interacts with non-neoplastic mucosa. While previous studies have focused on intratumoral regions or the invasive front, the biological organization of the interface remains poorly understood. We aimed to define spatially organized immune programs across the interface using single-cell–resolved spatial transcriptomics.

Methods

Using the Xenium platform, we analyzed matched tumor core and interface regions from 10 CRCs, including five microsatellite instability-high (MSI-H) and five microsatellite-stable (MSS) tumors. Key findings were supported by immunohistochemistry, immunofluorescence, a public scRNA-seq dataset of over 300 patients, and an independent public Xenium dataset.

Results

The lateral tumor–normal interface differed from the tumor core and contrasted with features reported at invasive fronts. Regardless of microsatellite status, the interface was characterized by enrichment of B cells and plasma cells, as well as CXCL14 expression toward the non-neoplastic mucosa. At the interface, cytotoxic lymphocyte populations and immune-associated niches were enriched in MSI-H tumors compared with MSS tumors. Within MSI-H tumors, CXCL9, CXCL10, and CXCL11 were more highly expressed in the tumor-associated region than in the non-neoplastic mucosa. Notably, MSS tumors were not uniformly immune-cold. A subset of MSS tumors showed higher T cell infiltration at the interface despite immune-depleted tumor cores. Additionally, cytotoxic immune features were present in the non-neoplastic mucosa adjacent to malignant epithelium in MSS tumors. In contrast, MSI-H tumors showed high cytotoxic scores within the tumor-associated region. These differences may be related to distinct multicellular

niches and inferred cell–cell interactions across microsatellite subtypes, including IL15–IL2RB interactions within tumor–CD8 T cell niches in MSI-H tumors and VEGFA–FLT1 interactions within endothelial niches in MSS tumors. Several key spatial patterns were supported by an independent spatial dataset.

Conclusions

Our findings suggest that the tumor–normal interface may serve as a spatial checkpoint in CRC, sharing common immune features irrespective of microsatellite status while revealing differences in immune organization between microsatellite subtypes. Differences between MSI-H and MSS tumors may reflect not only the magnitude of immune activation but also its spatial distribution across the interface. These results provide a framework for understanding immune organization in CRC and may inform future therapeutic strategies, particularly in MSS tumors.

Keywords: Colorectal cancer, Spatial transcriptomics, Immune microenvironment, Intercellular communication, Single-cell RNA sequencing

Introduction

Tumor progression in colorectal cancer (CRC) is not spatially uniform, and distinct biological programs emerge at defined tumor boundaries. Among these, the invasive front—where tumor cells infiltrate into deeper stromal compartments—has been extensively studied and is recognized as a critical site of tumor progression [1, 2]. This region is enriched for tumor budding, epithelial–mesenchymal transition (EMT)-like transcriptional programs, and stromal activation, and has been closely associated with metastatic potential and poor clinical outcome [3-5]. These features

collectively establish the invasive front as a key spatial niche driving tumor invasion and tissue remodeling.

However, tumor boundaries are not limited to the invasive front. In CRC, tumor glands also lie in direct apposition to adjacent non-neoplastic colonic mucosa and submucosa, forming a lateral tumor–normal interface. Under physiological conditions, the colonic mucosa maintains epithelial barrier integrity and rapid cell turnover, while the underlying lamina propria and submucosa support immune surveillance and tissue homeostasis through resident immune and stromal cell populations [6]. In this context, this tumor–normal interface represents a boundary where malignant epithelium directly encounters a functionally organized host tissue environment characterized by epithelial homeostatic programs and organized mucosal immune architecture. This stands in clear contrast to the invasive front, which is dominated by stromal and extracellular matrix remodeling. Despite its potential importance as a site of epithelial adaptation and host response, this region has received relatively limited attention, and most prior studies have focused on the invasive front or broadly defined tumor boundaries without resolving this lateral compartment as a distinct spatial entity.

Emerging evidence from other cancer types suggests that tumor boundary regions can constitute biologically distinct niches. In melanoma, spatial transcriptomic analysis identified interface-specific hybrid states at the tumor–microenvironment boundary [7]. More directly, in kidney cancer, single-cell transcriptomic mapping across intratumoral and tumor-associated territories identified discrete cellular and microenvironmental programs in tumor-adjacent regions, supporting the concept that tissues immediately bordering tumors are not merely transitional but functionally specialized compartments [8]. Whether a comparable, anatomically defined lateral tumor–normal interface exists and functions as a specialized immune niche in CRC, however, remains unclear.

Recent advances in spatially resolved transcriptomic technologies have enabled high-resolution mapping of cellular organization within intact tissues, shifting the focus from cell-type composition

to spatially organized cellular interactions that define functional niches within tumors [9, 10]. In this study, we applied high-resolution spatial transcriptomic profiling using the Xenium platform to delineate immune niches across the tumor core and the lateral tumor–normal interface in CRC, including both microsatellite stable (MSS) and microsatellite instability-high (MSI-H) tumors. By integrating spatial localization with cell-type–specific transcriptional states, we sought to define distinct immune programs associated with this underexplored boundary and to characterize spatially organized transitions in immune cell states across the tumor core–interface axis.

Methods

Patient cohort and tissue sampling

The study included 10 patients with colorectal cancer, comprising five MSI-H and five MSS cases. Paired tumor-core and tumor–normal interface samples were obtained from each patient using tissue microarray cores measuring 3 mm in diameter, yielding 20 cores in total. The clinicopathological characteristics of the cohort, including molecular and TNM classification data, are summarized in Table S1.

Sampling regions were manually selected by a pathologist through histological review. Tumor-core samples were obtained from intratumoral regions, whereas interface samples encompassed the lateral boundary between tumor tissue and adjacent non-invaded tissue. A small portion of adjacent normal mucosa was intentionally included in interface cores to preserve spatial orientation. Thus, “tumor–normal interface” refers to the sampled region encompassing this histological boundary, rather than a zone of predefined width. No algorithmic distance threshold or fixed interface width was applied.

Microsatellite instability (MSI) analysis

Microsatellite instability (MSI) testing was performed using a real-time PCR–based assay with the U-TOP MSI Detection Kit (Seasun Biomaterials, Daejeon, Korea) according to the manufacturer's instructions. Genomic DNA extracted from formalin-fixed paraffin-embedded (FFPE) tumor tissue was analyzed using five mononucleotide repeat markers (BAT-25, BAT-26, NR-21, NR-24, and NR-27). Tumors showing instability in two or more markers were classified as MSI-high (MSI-H), whereas tumors without instability or with instability in only one marker were classified as microsatellite stable (MSS).

PNA clamping real-time PCR for KRAS and NRAS mutation

KRAS and NRAS mutation analyses were performed using a peptide nucleic acid (PNA)-mediated real-time PCR clamping assay (PANAMutyper™ RAS Kit, Panagene Inc., Daejeon, Korea) according to the manufacturer's instructions. Genomic DNA extracted from FFPE tumor tissue was analyzed for hotspot mutations in KRAS (exon 2, codons 12 and 13; exon 3, codons 59 and 61; exon 4, codons 117 and 146) and NRAS (exon 2, codons 12 and 13; exon 3, codons 59 and 61; exon 4, codons 117 and 146). Mutation status was determined by selective amplification of mutant alleles using PNA-mediated real-time PCR clamping. The mutation status of each patient is summarized in Table S1. KRAS and NRAS mutation status was used to describe the cohort and was not included as a covariate or used to interpret the spatial analyses.

Xenium spatial transcriptomics experimental workflow

Slide preparation for Xenium analysis was performed according to the standard protocols established by 10x Genomics. Briefly, FFPE tissue samples were first sectioned and mounted onto Xenium slides following the manufacturer’s recommendations. Prior to Xenium assay execution, tissue quality assessment, deparaffinization, and decrosslinking were completed. The Xenium assay was conducted using the Xenium Human Immuno-Oncology Profiling Panel (PN-1000654) following the Xenium In Situ Gene Expression User Guide (CG000582). After

completion of the assay workflow, the slides were loaded onto the Xenium instrument for imaging and data acquisition following the Xenium Analyzer User Guide (CG000584). The panel comprises 380 genes. The complete gene list downloaded from the 10x Genomics website, together with an overview of the major pathways and cell types covered, is provided in Table S2.

Xenium data processing, clustering and cell-type annotation

The raw count matrix generated by the Xenium Analyzer was processed using the Seurat package (v5.3.1) [11] in R (v4.4.2). Low-quality cells were excluded based on the 10x Xenium analysis guidelines, retaining cells with nCount_Xenium ≥ 20 and ≤ the 98th percentile of nCount_Xenium. The data were normalized using the SCTransform function. Principal component analysis (PCA) was applied for dimensionality reduction. Clustering was subsequently performed by computing the shared nearest-neighbor graph using the top 30 principal components, followed by cell clustering using the Louvain algorithm (resolution = 0.2). Visualization of the results was achieved using Uniform Manifold Approximation and Projection (UMAP). Cell types were assigned on the basis of the expression of known marker genes. For subclustering of each major cell identity, the process was repeated starting with the PCA step.

Differential abundance analysis using Milo

For differential abundance analysis, we used miloR (v1.10.0) [12]. K-nearest neighbor (KNN) graphs were constructed in PCA space using the buildGraph function, with parameters selected according to annotation resolution. For major cell-type-level analyses, graphs were generated using d = 25 and k = 10, whereas subtype-level analyses used d = 20 and k = 20. Cellular neighborhoods were then defined using the makeNhoods function, and the number of cells within each neighborhood across samples was quantified using countCells. Differential abundance testing was performed using testNhoods with a spatial false discovery rate (FDR) threshold of 0.10. In all analyses, each sample was treated as the unit of replication in the negative binomial

generalized linear model implemented in Milo. Specifically, MSI-H versus MSS comparisons were performed separately for the tumor core and interface regions. Within each region, neighborhood cell counts were aggregated by patient ID, with each patient serving as an independent biological replicate (n = 5 per group), and differential abundance was tested using design = ~ MSI_status. For tumor core versus interface comparisons, cell counts were aggregated separately for each patient–region combination using sample IDs. Because both regions were obtained from the same patients, patient ID was included as a blocking factor to account for paired sampling and between-patient variability (design = ~ PatientID + Region). The same model designs were used when the interface was restricted to the tumor-associated region.

Patient-level analysis

To assess whether compositional differences were driven by individual patients, the proportion of each cell type and cellular neighborhood was calculated for each patient and region using the same denominators as in the corresponding Milo analyses. First, differences were oriented so that positive values indicated the direction observed in the corresponding Milo analysis. The Hodges–Lehmann estimate (the median of all pairwise differences between MSI-H and MSS tumors, or the Hodges–Lehmann estimate of paired differences) was recalculated after excluding each patient in turn. Comparisons with a positive overall estimate were flagged if excluding any single patient yielded an estimate of zero or a negative value. Second, the mean difference was recalculated after excluding the patient with the highest proportion in the group indicated by the Milo analysis as having higher abundance (for paired comparisons, the patient with the largest paired difference in the direction indicated by the Milo analysis). Comparisons with a positive overall mean difference were flagged if this exclusion yielded a mean difference of zero or a negative value. Differences flagged by either approach were considered possibly driven by a single patient. Comparisons in which the overall Hodges–Lehmann estimate or mean difference was not in the direction indicated by the Milo analysis were classified separately. Table S3

summarizes patient-level directional checks for 90 comparisons of major cell types, cell subtypes, and cellular neighborhoods. For these comparisons, findings that failed the directional checks were omitted or explicitly qualified in the Results. The heavy-chain isotype comparisons in Figure 3I were exploratory.

Spatial area estimation of tumor core and interface sections

For each sample, a concave hull polygon was generated from cell centroid coordinates using the concaveman package (v1.2.0) [13] in R. The polygon area was calculated using the st_area function in the sf package (v1.1-2) [14] and converted from μm² to mm².

Spatial immunotype classification based on $CD3^+$ and $CD8^+$ T cell densities

In colorectal cancer, the consensus Immunoscore, which integrates $CD3^+$ and $CD8^+$ T cell densities from the tumor core and invasive margin, is an internationally validated method for assessing immune infiltration [15]. Previous studies have also employed cohort-specific, distribution-based thresholds to classify T cell infiltration [16-18]. Based on these approaches, we exploratorily classified each region according to the distribution of $CD3^+$ and $CD8^+$ T cell densities in our cohort, allowing comparison between the tumor core and the tumor–normal interface. The cutoff for each marker was defined as the median density across all 20 regions ($CD8^+$, 365 cells/mm²; $CD3^+$, 777 cells/mm²). Regions with both $CD3^+$ and $CD8^+$ T cell densities at or above the cutoffs were classified as immune-enriched, those with only one as immune-intermediate, and those with neither as immune-depleted.

Heavy-chain isotype annotation

Heavy-chain isotype annotation was performed based on the expression of immunoglobulin heavy chain genes, following previously described methods [19]. In the Xenium data, the genes included in the panel (IGHG1, IGHG2, IGHG3, IGHG4, and IGHM) were used; IGHA1, IGHA2,

IGHD, and IGHE were not included in the panel. In the independent scRNA-seq dataset, IGHA1, IGHA2, IGHD, and IGHE were additionally used.

Independently of the clustering-based plasma cell subtype annotation, immunoglobulin heavy-chain isotypes were assigned to individual plasma cells based on the gene with the highest expression level. Cells without detectable heavy-chain transcripts or with ties in maximal expression across multiple isotype genes were classified as isotype-unassigned plasma cells.

Immunohistochemistry and immunofluorescence

Immunohistochemistry for IgG was performed on FFPE tissue sections using a rabbit polyclonal anti-IgG antibody (Cell Marque, Rocklin, CA, USA) at a dilution of 1:500. Staining was performed using a BenchMark XT autoimmunostainer (Ventana Medical Systems, Tucson, AZ, USA) according to the manufacturer's protocol.

Dual immunofluorescence staining for IL15 and pan-cytokeratin (Pan-CK) was performed on FFPE tissue sections using anti-human IL15 antibody (AF315-SP; R&D Systems, Minneapolis, MN, USA) and anti-Pan-Cytokeratin antibody (clone AE-1/AE-3; 914204; BioLegend, San Diego, CA, USA). Images were acquired using a Nikon AX R confocal microscope (Nikon, Tokyo, Japan).

Spatial trajectory inference

Spatial trajectory analysis was performed using the SPATA2 package (v3.1.4) [20] in R to investigate transcriptional dynamics across tissue regions. A pathologist annotated the tumor-associated region and non-neoplastic mucosa within each interface sample and defined the spatial trajectory path. These pathologist-defined trajectories were then manually implemented in R using the createSpatialTrajectories function, extending from the tumor-associated region toward the non-neoplastic mucosa. To distinguish interface features from those of the non-neoplastic mucosa, the analysis was repeated within the tumor-associated region only, with trajectories running from its core-proximal edge to its mucosa-proximal edge, adjacent to the non-

neoplastic mucosa. Custom gene sets were curated based on Gene Ontology (GO) terms [21], using "GOBP_GRANZYME_MEDIATED_PROGRAMMED_CELL_DEATH_SIGNALING_PATHWAY" for the cytotoxic score and "GOBP_CELL_CHEMOTAXIS" for the chemotaxis score. Both gene sets were restricted to genes included in the Xenium panel. The chemotaxis gene set was further restricted to chemokine genes. For each cell, SPATA2 calculated signature scores as the mean expression values of the corresponding signature genes in the active expression matrix. Cells within the trajectory frame were projected onto the spatial trajectory to determine their distances from the trajectory origin. Signature scores were then modeled as a function of distance using locally estimated scatterplot smoothing (LOESS). The fitted LOESS model was used to estimate signature scores at representative positions along the trajectory, determined from distance bins based on the spatial resolution. Changes in signature scores and gene expression along these trajectories were visualized using the plotStsLineplot, plotStsHeatmap, and plotSurface functions. The gene sets used to calculate the signature scores are provided in Table S4.

Cellular neighborhood (CN) identification

We applied the cellular neighborhood identification method established in previous studies [22]. To define CNs, windows were constructed for each index cell by including neighboring cells within a radius of 18.85 μm. For subsequent analysis, we only considered windows with a size larger than five cells (including the index cell). The median number of cells per window was 13 (interquartile range, 10-18), including the index cell, and sample-level medians ranged from 9 to 19 (Figure S8A). Cell subtype proportions were calculated within each window and used for clustering and the final annotation of CNs.

Inference of cell–cell communication using LIANA+

LIANA+ (v1.3.0) [23] was used to infer cell–cell communication between co-existing cell subtypes. For intra-CN cell–cell communication analysis, we selected all cells within each CN to create an independent AnnData object to be used as input. To identify co-expressed ligand–receptor (L–R) pairs in the CellPhoneDB [24], CellChat [25] and ConnectomeDB2020 [26] databases, the "mt.rank_aggregate" function was run with the parameter "expr_prop=0.05". This calculates L–R scores for each L–R pair between each pair of cell types using multiple methods, namely CellPhoneDB, Connectome, NATMI, log2FC, and SingleCellSignalR [27]. The scores from the different tools were aggregated into a *P* value for magnitude (strength of the interaction) and a *P* value for specificity (compared to other pairs of clusters) of a given L–R interaction between two cell types using robust rank aggregation.

To quantify the spatial strength of L–R interactions, we computed inflow scores using the mt.inflow function (expr_prop = 0.05). Spatial connectivity was modeled using a Gaussian kernel with an adaptive bandwidth determined separately for each sample, such that each cell had approximately 5 neighboring cells. Statistical significance was assessed using 1,000 permutations.

Analysis of an independent colorectal cancer scRNA-seq atlas

The scRNA-seq dataset was processed using Seurat in R. The CRC atlas [28] was downloaded from the CRC atlas project website, and samples from the tumor tissue were extracted. To annotate CD8 T cell and CD4 T cell subtypes, preprocessing and clustering were conducted on T/NK cells. The filtered expression profile was normalized and scaled by a factor of 10,000 and then log-transformed. The author-provided scANVI latent representation was used to construct the shared nearest-neighbor graph and perform UMAP dimensionality reduction. Leiden clustering (resolution = 0.8) was then performed to generate T/NK subclusters. T/NK cell annotation was performed based on the expression of common canonical marker genes.

Analysis of an independent public Xenium dataset

To assess key spatial findings in an independent dataset, we analyzed a publicly available Xenium dataset of colorectal cancer (E-GEAD-1117) [29], which was generated with the Xenium Human 5K Pan Tissue & Pathways Panel and includes interface region and microsatellite status annotations. Microsatellite status in this dataset was reported as MSI or MSS, without distinguishing MSI-H from MSI-L. We therefore retain the original MSI label for this dataset. Among the samples in this dataset, one MSI and one MSS tumor contained the tumor core, the tumor–normal interface, the distal tumor region and the distal normal region and were analyzed. In the MSS tumor, two interface regions within the same tissue section were analyzed separately (MSS interfaces 1 and 2); because they were derived from the same tumor, they were not treated as independent replicates. As in the in-house data, interface regions were annotated into non-neoplastic mucosa and tumor-associated region. All regions were annotated by a pathologist. Data were processed using the same pipeline as the in-house data, including SCTransform normalization and clustering (resolution = 0.4), and cell types were annotated independently based on canonical marker genes. Clusters without sufficient marker genes were annotated as "Unidentified."

Statistical analysis

All statistical analyses were performed using R (v4.4.2). Unless otherwise specified, *P* values were calculated using an unpaired two-tailed Welch's *t*-test for comparisons between two independent groups or a paired two-tailed *t*-test for paired samples, depending on the experimental design. Effect sizes for comparisons of T cell densities between MSI-H and MSS tumors were estimated as mean differences and Cohen's d with 95% confidence intervals, and P values were adjusted for the two regional comparisons for each marker using the Benjamini–Hochberg method. Patient-level dependence of compositional differences was assessed using Hodges–Lehmann estimates and mean differences, as described in "Patient-level analysis."

Clinical samples were selected based on microsatellite status and tissue availability, comprising paired tumor core and tumor–normal interface specimens from five MSI-H and five MSS colorectal tumors. No formal sample size calculation was performed. Randomization and blinding were not applicable because this was an observational study using archived human tissue specimens.

Ethics approval and consent to participate

The study was approved by the Institutional Review Board of Ajou University Hospital (IRB No. AJOUIRB-KS-2026-329). The requirement for informed consent was waived owing to the retrospective nature of the study and the use of archived formalin-fixed paraffin-embedded tissue specimens and de-identified clinical data. All procedures were performed in accordance with the Declaration of Helsinki and relevant institutional guidelines and regulations.

Results

High-resolution spatial transcriptomics reveals distinct cellular ecosystems across tumor core and tumor–normal interface regions in colorectal cancer

To systematically characterize the spatial organization of colorectal cancer ecosystems, we performed single-cell–resolved spatial transcriptomic profiling of paired tumor core and tumor–normal interface regions from MSI-H and MSS colorectal cancers (Figure 1A). Using the Xenium In Situ platform (10x Genomics), we analyzed 20 spatial regions from 10 patients (five MSI-H and five MSS), generating spatial maps comprising 1,312,830 cells across a 380-gene panel. Unsupervised clustering followed by annotation based on canonical marker genes identified nine major cell populations, including epithelial, fibroblast, endothelial/mural, T/NK, B, plasma, myeloid, mast, and enteric glial cells (Figure 1B-C). Histologic examination and spatial cell-type mapping demonstrated substantial cellular heterogeneity across both tumor core and interface regions in MSI-H and MSS tumors (Figure 1D, Figure S1A-B).

We then examined the distribution of major cell populations across tumor core and interface regions. Given the small cohort size, we focused on differences that were significant in the differential abundance analysis and retained their direction in the patient-level sensitivity analyses (Methods and Table S3). Differential abundance analysis using Milo revealed preferential enrichment of B cells and plasma cells at the tumor–normal interface, whereas fibroblasts and myeloid cells were enriched in the tumor core (Figure S1C). Microsatellite status-specific results are provided in Figure S1D–E. To assess whether this pattern reflected the inclusion of non-neoplastic mucosa, we repeated the analysis after restricting the interface to the tumor-associated region (Figure S2A). After this restriction, B cells and plasma cells remained enriched at the interface, whereas fibroblasts and myeloid cells remained enriched in the tumor core (Figure S2B). The persistence of B-cell and plasma-cell enrichment suggests that their accumulation at the interface was not solely explained by the inclusion of non-neoplastic mucosa. We next compared region-matched MSI-H and MSS samples and found marked differences in cellular composition according to microsatellite status. At the interface regions, MSI-H tumors were enriched for immune populations, including plasma cells, T/NK cells, and myeloid cells, whereas MSS tumors were enriched for fibroblast and endothelial/mural populations in both the interface and tumor core regions (Figure 1E-F). These findings indicate that microsatellite status is associated with broad differences in immune and stromal composition across spatial compartments, most prominently at the interface.

Figure 1

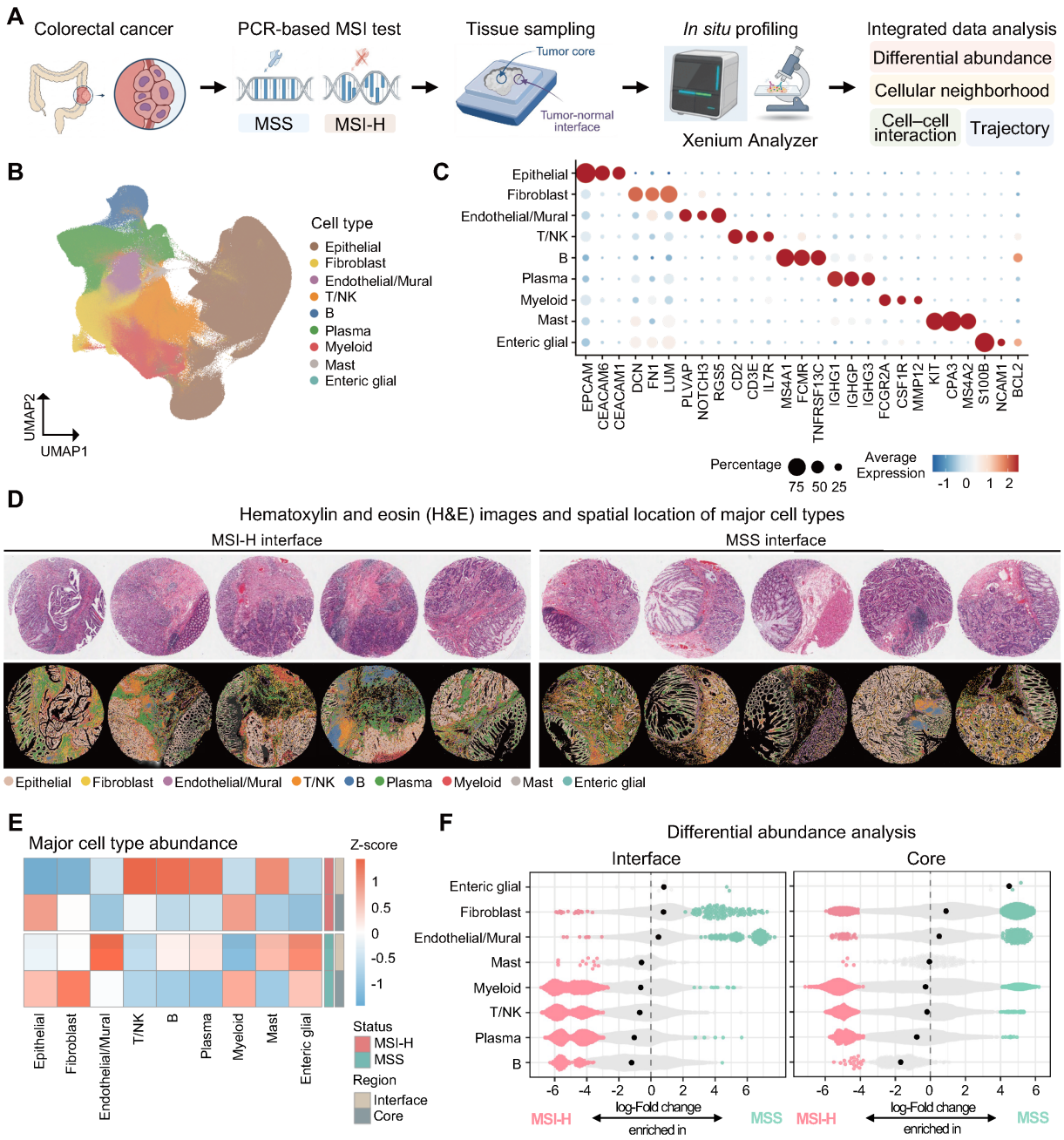

Figure 1. Spatial profiling of MSI-H and MSS colorectal tumors by single-cell–resolved transcriptomics

A, Schematic overview of the study design. Primary tumor cores and matched interface regions from MSI-H and MSS colorectal cancer patients were profiled using the Xenium platform, followed

by cell-type annotation and spatial analyses. **B**, UMAP visualization of major cell types identified from Xenium data. **C**, Dot plot showing canonical marker gene expression across annotated cell types. Dot size represents the fraction of expressing cells and color indicates scaled average expression. **D**, Hematoxylin and eosin (H&E) images (top) and spatial maps showing the distribution of major cell types across interface regions (bottom) in MSI-H and MSS samples. **E**, Heatmap of Z-scored major cell type proportions across microsatellite status and spatial regions. **F**, Differential abundance analysis of major cell types using Milo, comparing MSI-H with MSS tumors within the interface and tumor core regions. Log_2 fold changes are shown for each cell type (spatial FDR < 0.1).

Spatial organization of T cell states reveals interface-specific immune heterogeneity in MSS colorectal cancer

To characterize the spatial organization of T cell states in colorectal cancer, we analyzed the T cell compartment across tumor core and tumor–normal interface regions in MSI-H and MSS tumors. Within the T cell compartment (n = 159,633), we identified seven subsets based on canonical marker expression, including naïve $CD4^+$ T cells, $CXCL13^+$ CD4 T cells, regulatory T (Treg) cells, naïve $CD8^+$ T cells, tissue-resident memory CD8 T cells (CD8 Trm), $GZMK^+$ CD8 effector memory T cells ($GZMK^+$ CD8 Tem), and $GNLY^+$ CD8 effector T cells (Figure 2A-C). Differential abundance analysis revealed preferential enrichment of multiple effector-associated T cell populations in MSI-H tumors across both tumor core and interface regions (Figure 2D). In particular, CD8 Trm, $CXCL13^+$ CD4 T cells, and $GNLY^+$ CD8 effector T cells were significantly enriched in MSI-H samples. By contrast, Treg cells showed enrichment in MSS tumor core compared to MSI-H tumor core. MSS tumors also exhibited greater spatial segregation of naïve and regulatory T cell states, with naïve $CD4^+$ T cells preferentially localized to interface regions

and Treg cells enriched within tumor regions (Figure 2E). Representative spatial maps further illustrated these patterns, with prominent accumulation of GNLY$^+$ CD8 effector T cells along the tumor–normal interface in MSI-H tumors, whereas Treg cells showed preferential localization within the core regions in MSS tumors (Figure 2F-G, Figure S4A-B). Collectively, these findings suggest that, although MSS tumors generally display a less inflamed T cell landscape, the tumor–normal interface was enriched for naïve CD4$^+$ T cell populations, whereas tumor core regions are characterized by relative accumulation of regulatory T cells. Moreover, the enrichment of these populations was preserved when the interface was restricted to the tumor-associated region (Figure S2C).

To further characterize immune infiltration patterns, we classified each region based on CD3$^+$ and CD8$^+$ T cell densities. Consistent with the highly immunogenic nature of MSI-H colorectal cancer [10, 30], CD3$^+$ and CD8$^+$ T cell densities tended to be higher in MSI-H than in MSS tumors in both regions (Figure 2H). At the interface, the mean difference in CD8$^+$ T cell density was 512 cells/mm² (Cohen's d = 1.80, 95% CI for d 0.25–3.28). The adjusted P value for this comparison was 0.064, and none of the four density comparisons reached statistical significance after Benjamini–Hochberg correction across the two regions for each marker (Table S5B). We used the median density of each marker across all 20 regions in our cohort as its threshold (777 cells/mm² for CD3$^+$ and 365 cells/mm² for CD8$^+$). A higher proportion of MSI-H than MSS samples met both thresholds and were classified as immune-enriched at the interface and in the tumor core (Figure 2I). In contrast, MSS tumors exhibited substantial spatial heterogeneity. Two MSS cases showed a higher immune classification at the interface than in the tumor core, suggesting relative immune accumulation at the tumor–normal interface in these cases (Figure 2I, Table S5A). Conversely, one MSS case showed the opposite pattern, with an immune-intermediate tumor core and an immune-depleted interface (Table S5A). These findings suggest that immune activity at the

tumor–normal interface is not necessarily reflected by the immune status of the tumor core, highlighting the interface as a distinct immune microenvironment within colorectal cancer.

Figure 2

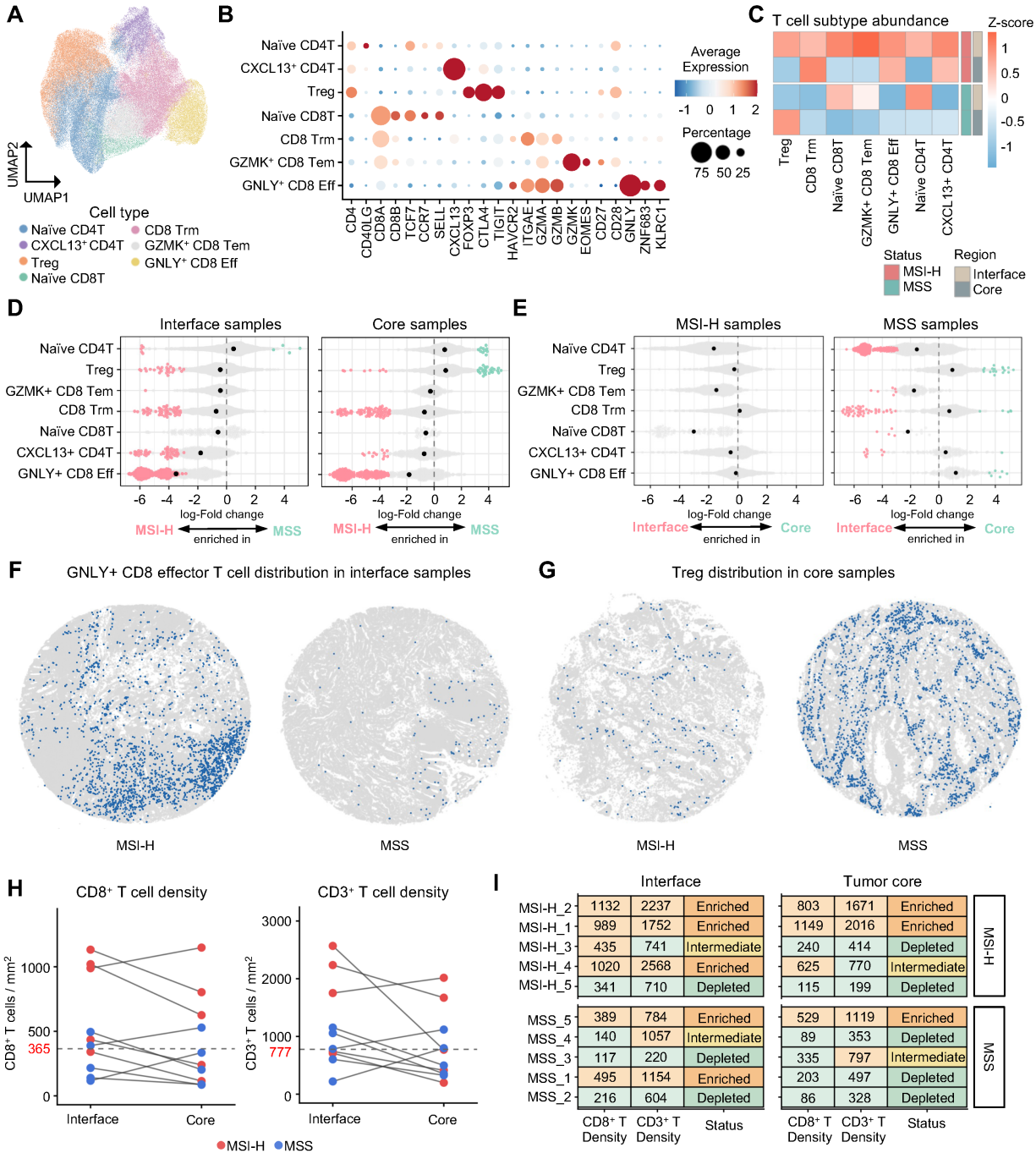

Figure 2. T cell immune landscapes in MSI-H and MSS colorectal tumors

A, UMAP visualization of T/NK cell subsets identified from Xenium data. **B**, Dot plot showing marker gene expression across T/NK cell subsets. **C**, Heatmap of Z-scored T/NK cell subset proportions across microsatellite status and spatial regions. **D,E**, Differential abundance analysis of T/NK cell subsets comparing MSI-H and MSS conditions within interface and tumor core regions (D), and comparing tumor core and interface regions within MSI-H and MSS samples (E). **F,G**, Spatial distribution of representative T cell subsets. $GNLY^+$ CD8 effector T cells and regulatory T cells (Tregs) are shown. **H**, $CD8^+$ and $CD3^+$ T cell densities in the interface and tumor core regions. Dots represent individual patients, and black lines connect matched interface and tumor core samples from the same patient. **I**, Exploratory spatial immune classification based on $CD8^+$ and $CD3^+$ T cell densities in the interface and tumor core of individual patients. Regions were classified as enriched (both densities ≥ cohort median), immune-intermediate (one density ≥ cohort median), or depleted (both densities below cohort median). Cell densities are expressed as cells/mm².

Plasma cell programs at tumor core and interface regions are linked to MSI-H and immune-responsive states

To extend our analysis to humoral immune components, we next examined the spatial distribution of plasma cell populations across tumor compartments. Unsupervised clustering identified four plasma-related subsets: plasma not otherwise specified (plasma NOS), IgG^+ plasma, IgM^+ plasma and plasma–stromal cells (Figure 3A and C). Among these, the plasma NOS was defined as cells lacking clear enrichment of either IgG or IgM markers, whereas the plasma–stromal population was defined by co-expression of plasma cell markers together with stromal markers including DCN and FN1 (Figure 3B). Comparison of plasma cell subtype abundance revealed distinct subtype compositions according to microsatellite status. At the interface, MSI-H tumors were enriched for IgG^+ plasma and plasma–stromal populations, whereas plasma NOS cells were

more prevalent in MSS tumors (Figure 3C-D). However, despite these differences, differential abundance analysis revealed broadly similar localization patterns across microsatellite subtypes (Figure 3E). In both MSI-H and MSS tumors, plasma NOS and IgM^+ plasma cells were enriched at the interface relative to the tumor core, but these regional differences were no longer significant after excluding non-neoplastic mucosa (Figure S3A). This may reflect the localization of these subsets in the non-neoplastic mucosa. In comparisons between MSI-H and MSS tumors within the tumor-associated region of the interface, IgG^+ plasma cells were enriched in MSI-H tumors, whereas plasma NOS cells were enriched in MSS tumors (Figure S3A). Spatial mapping showed that the overall abundance of IgG^+ plasma cells was markedly lower in MSS tumors than in MSI-H tumors (Figure 3F, Figure S3B). This was further validated by IgG immunohistochemistry (Figure 3G, Figure S3C). These results show that MSI-H and MSS tumors differ in the abundance of plasma cell subsets. Because IGHA1 and IGHA2 were not in the panel, IgA-producing cells could not be identified. Plasma NOS cells, which expressed JCHAIN without IgG or IgM transcripts (Figure 3B), may include them, but their identity and abundance could not be determined using this panel.

To further characterize plasma cell states, we examined immunoglobulin heavy-chain isotype usage within the Xenium dataset. MSI-H tumors showed a higher proportion of IgG-expressing plasma cells, whereas MSS tumors contained a larger fraction of isotype-unassigned plasma cells and $IGHM^+$ plasma cells (Figure 3H). Differential abundance analysis further revealed region-specific isotype distributions: at the tumor–normal interface, $IGHG1^+$, $IGHG2^+$, and $IGHG3^+$ plasma cells were enriched in MSI-H tumors. Within tumor core regions, enrichment was largely restricted to the $IGHG2^+$ plasma cell subset in MSI-H tumors (Figure 3I). To validate these findings, we analyzed an independent colorectal cancer single-cell atlas containing clinical annotation of microsatellite status and response to immune checkpoint blockade [28]. Using the original authors' annotations, plasma cells were classified into plasma IgA, plasma IgG, plasma IgM, and

plasmablast populations (Figure 3J). MSI-H tumors exhibited a higher proportion of IgG plasma cells, whereas MSS tumors showed relative expansion of IgA plasma cells (Figure 3K). Because IgA could not be measured in the Xenium data, this MSS-associated IgA pattern is supported by the scRNA-seq atlas alone. Consistent with the Xenium analysis, differential abundance analysis confirmed enrichment of $IgG1^+$ and $IgG2^+$ plasma cells in MSI-H tumors and IgM^+ plasma cells in MSS tumors (Figure 3L). Notably, the interface-associated enrichment of $IgG3^+$ plasma cells in MSI-H tumors observed in the spatial dataset was not recapitulated in the independent single-cell atlas. This discrepancy may reflect the localization of this population to the tumor–normal interface, which may not be captured by dissociation-based sampling, but may also reflect differences in cell abundance, cohort composition or platform.

To further assess the potential biological relevance of $IgG3^+$ plasma cells, we next examined the association between plasma cell isotypes and response to immune checkpoint inhibitors (ICIs) within the same single-cell atlas. Although present at relatively low abundance, $IgG3^+$ plasma cells were enriched in pre-treatment responder samples compared with non-responders, alongside a prominent enrichment of $IgG1^+$ plasma cells (Figure 3M). These findings raise the possibility that the interface-associated $IgG3^+$ plasma cell population identified by spatial transcriptomics may be linked to effective antitumor immune responses.

Figure 3

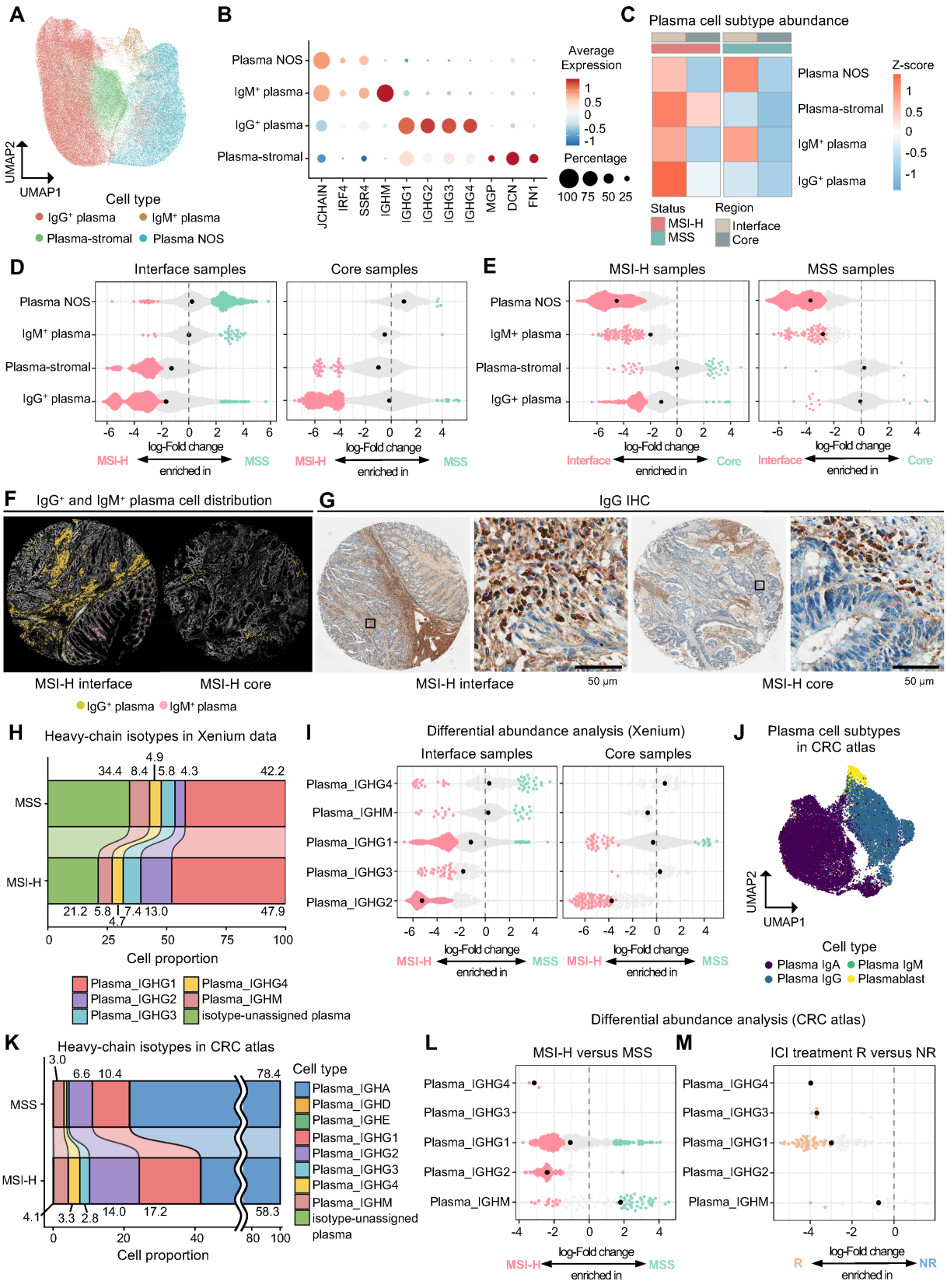
A
UMAP2
UMAP1
Cell type
IgG+ plasma
IgM+ plasma
Plasma-stromal
Plasma NOS
B
Plasma NOS
IgM+ plasma
IgG+ plasma
Plasma-stromal
JCHAIN
IRF4
SSR4
IGHM
IGHG1
IGHG2
IGHG3
IGHG4
MGP
DCN
FN1
Average Expression
Percentage
100 75 50 25
C
Plasma cell subtype abundance
Z-score
Status
MSI-H
MSS
Region
Interface
Core
D
Interface samples
Core samples
log-Fold change
MSI-H
enriched in
MSS
E
MSI-H samples
MSS samples
Interface
Core
F
IgG+ and IgM+ plasma cell distribution
MSI-H interface
MSI-H core
G
IgG IHC
50 μm
H
Heavy-chain isotypes in Xenium data
Cell proportion
Plasma_IGHG1
Plasma_IGHG2
Plasma_IGHG3
Plasma_IGHG4
Plasma_IGHM
isotype-unassigned plasma
I
Differential abundance analysis (Xenium)
J
Plasma cell subtypes in CRC atlas
Plasma IgA
Plasma IgM
Plasma IgG
Plasmablast
K
Heavy-chain isotypes in CRC atlas
Plasma_IGHA
Plasma_IGHD
Plasma_IGHE
L
Differential abundance analysis (CRC atlas)
MSI-H versus MSS
M
ICI treatment R versus NR
R
NR

Figure 3. Plasma cell programs at tumor core and interface regions

A, UMAP visualization of plasma cell subsets, including plasma NOS, IgG^+ plasma, IgM^+ plasma and plasma–stromal. **B**, Dot plot showing marker gene expression across plasma cell subsets. **C**, Heatmap of Z-scored plasma cell subset proportions across microsatellite status and spatial regions. **D,E**, Differential abundance analysis of plasma cell subsets comparing MSI-H and MSS conditions within interface and tumor core regions (D), and comparing tumor core and interface regions within MSI-H and MSS samples (E). Log_2 fold changes are shown (spatial FDR < 0.1). **F**, Spatial mapping of plasma cell subsets across MSI-H tumor core and interface regions. **G**, Representative IgG immunohistochemical staining of tumor core and tumor–normal interface in human MSI-H colorectal cancer. Scale bar represents 50 μm. **H**, Bar plots showing the proportion of plasma cell isotypes based on immunoglobulin heavy chain expression in Xenium data. **I**, Differential abundance analysis of isotype-level plasma cell annotations in the Xenium data comparing MSI-H and MSS conditions within interface and tumor core regions. **J**, UMAP displaying annotation of plasma cell subtypes in the CRC atlas. **K**, Bar plots showing the proportion of plasma cell isotypes based on immunoglobulin heavy chain expression in the CRC atlas. **L**, Differential abundance analysis of isotype-level plasma cell annotations in the CRC atlas comparing MSI-H and MSS conditions. **M**, Differential abundance analysis of isotype-level plasma cell annotations in pre-treatment samples. R, responder; NR, non-responder.

Distinct spatial organization of myeloid and fibroblast populations across tumor core and interface regions

Next, we analyzed the myeloid cell distribution across tumor core and interface regions. Within the myeloid compartment (n = 122,140), we identified five subsets based on canonical marker expression (Figure 4A-B, Figure S3D). At the interface, neutrophils were enriched in MSI-H

relative to MSS tumors, whereas dendritic cells were enriched in MSS tumor core compared to MSI-H tumor core (Figure 4C). Representative spatial maps illustrate the distribution of CCR7$^+$ macrophages at the interface in MSI-H and MSS tumors (Figure 4D, Figure S4C). Notably, within MSI-H tumors, differential abundance analysis showed preferential enrichment of CCR7$^+$ macrophages at the interface compared with the tumor core (Figure 4E). In contrast, in MSS tumors, C1QB$^+$ macrophages were enriched in the tumor core relative to the interface. The enrichment of these populations was preserved when the interface was restricted to the tumor-associated region (Figure S3F).

We then characterized fibroblast populations. Within the fibroblast compartment, we identified seven fibroblast subsets based on canonical marker expression (Figure 4F-G, Figure S3E). Differential abundance analysis revealed marked differences in fibroblast subset abundance according to microsatellite status. At the interface, CCL21$^+$ and IL6$^+$ fibroblasts were enriched in MSI-H tumors (Figure 4H), and both differences were preserved within the tumor-associated region (Figure S3G). Milo analysis also indicated enrichment of MGP$^+$, SPARCL1$^+$, CXCL14$^+$, and SDC1$^+$ fibroblasts in MSS tumors at the interface. However, these differences were possibly driven by a single patient (Table S3).

In the tumor core, IL6$^+$ fibroblasts were enriched in MSI-H tumors, whereas SPARCL1$^+$ and CXCL14$^+$ fibroblasts were enriched in MSS tumors. Spatial distribution mapping confirmed prominent accumulation of IL6$^+$ fibroblasts at the tumor–normal interface, particularly in MSI-H tumors (Figure 4I, Figure S4D). Differential abundance analysis further demonstrated consistent compartmentalization of fibroblast subsets across microsatellite subtypes, with IL6$^+$ fibroblasts enriched at the tumor–normal interface and SDC1$^+$ fibroblasts enriched within tumor cores (Figure 4J). When the interface was restricted to the tumor-associated region, IL6$^+$ fibroblast enrichment was preserved, whereas SDC1$^+$ fibroblast enrichment in the tumor core was attenuated in MSS tumors (Figure S3G). Together, these findings indicate that IL6$^+$ fibroblast enrichment at the

interface was shared across microsatellite subtypes, whereas macrophage compartmentalization differed by microsatellite status, with $CCR7^+$ macrophages enriched at the MSI-H interface and $C1QB^+$ macrophages enriched in the MSS tumor core.

Figure 4

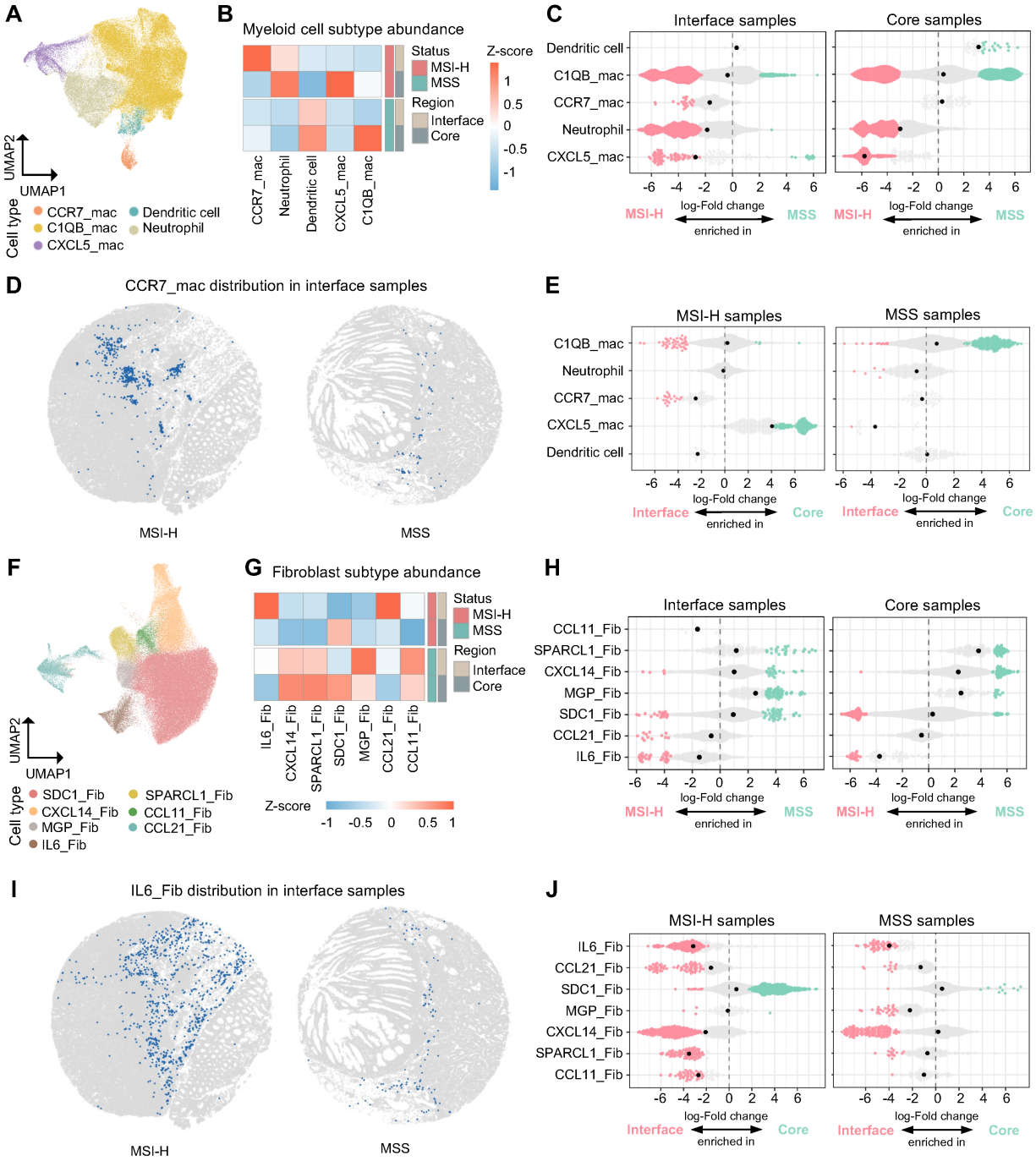

Figure 4. Myeloid and fibroblast heterogeneity across MSI-H and MSS tumors

A, UMAP visualization of myeloid cell subsets. **B**, Heatmap of Z-scored myeloid cell subset proportions across microsatellite status and spatial regions. **C**, Differential abundance analysis of

myeloid subsets comparing MSI-H and MSS conditions within interface and tumor core regions. Negative $\log_2$ fold changes indicate enrichment in MSI-H samples, and positive values indicate enrichment in MSS samples. **D**, Spatial mapping of $CCR7^+$ macrophages across MSI-H and MSS interface samples. **E**, Differential abundance analysis of myeloid subsets comparing tumor core and interface regions within MSI-H and MSS samples. **F**, UMAP visualization of fibroblast subsets. **G**, Heatmap of Z-scored fibroblast subset proportions across microsatellite status and spatial regions. **H**, Differential abundance analysis of fibroblast subsets comparing MSI-H and MSS conditions within interface and tumor core regions. **I**, Spatial mapping of $IL6^+$ fibroblasts across MSI-H and MSS interface regions. **J**, Differential abundance analysis of fibroblast subsets comparing tumor core and interface regions within MSI-H and MSS samples.

Spatial trajectory analysis reveals distinct chemokine and cytotoxic activation gradients across the tumor–normal interface

To investigate spatial immune organization across the tumor–normal interface, we performed trajectory analysis using SPATA2 [20] and projected curated chemotaxis and cytotoxic activation gene signatures along the spatial axis. Trajectory analysis was performed across the entire interface, including the tumor-associated region and the non-neoplastic mucosa. To distinguish interface features from those of the non-neoplastic mucosa, we repeated the analysis within the tumor-associated region only. In this restricted analysis, trajectories ran from the core-proximal edge to the mucosa-proximal edge of the tumor-associated region. MSI-H tumors exhibited sustained chemotaxis scores across both tumor-associated region and non-neoplastic mucosa (Figure 5A-C, Figure S5A). CXCL9, CXCL10, and CXCL11, key chemokines associated with recruitment of $CD8^+$ T cells, NK cells, and Th1 cells [31], were enriched in the tumor-associated region in MSI-H tumors (Figure 5D, Figure S5B). In contrast, MSS tumors showed low chemotaxis activity within the tumor-associated region that increased sharply toward the non-neoplastic

mucosa (Figure 5A-C, Figure S5A). This increasing trend in MSS tumors was preserved within the tumor-associated region (Figure S6A). Regardless of microsatellite status, CCL15 and CCL28 were preferentially expressed toward the non-neoplastic mucosa. However, this pattern was no longer observed after excluding non-neoplastic mucosa, suggesting that it reflected normal mucosal biology (Figure S5B, Figure S6B). In contrast, CXCL12 and CXCL14 were frequently elevated toward the non-neoplastic mucosa side even within the tumor-associated region in both MSI-H and MSS tumors (Figure S5B, Figure S6B), suggesting preservation of a shared interface-associated chemokine program.

We also examined the spatial distribution of cytotoxic scores across the tumor–normal interface. MSI-H tumors maintained high cytotoxic scores within tumor-associated regions, accompanied by coordinated expression of cytotoxic effector genes (Figure 5E-F, Figure S7A-B). This gradient was retained after restricting the analysis to the tumor-associated region (Figure S7C-D). In contrast, MSS tumors exhibited relatively low cytotoxic activation within tumor-associated regions but showed increased cytotoxic activation toward the non-neoplastic mucosa (Figure 5E-F, Figure S7A). This increase was no longer observed after excluding non-neoplastic mucosa, suggesting that the mucosal compartment contributed to the original gradient (Figure S7C). Thus, within the tumor-associated region of MSS tumors, chemotactic signals increasing toward its mucosa-proximal edge were not accompanied by a corresponding increase in cytotoxic activation.

However, this pattern was not uniform across MSS tumors. Notably, one MSS tumor exhibited a reversed spatial pattern, maintaining elevated cytotoxic activation within the tumor-associated region rather than the non-neoplastic mucosa (Figure 5G-I). This inflamed phenotype was accompanied by prominent CXCL16 expression together with broad induction of cytotoxic effector genes. CXCL16 has been implicated in the retention and maintenance of $CXCR6^{+}$ cytotoxic lymphocytes within tumors [32], suggesting a potential link between local chemokine expression and intratumoral immune activation. Together, these findings indicate that MSS tumors are not

uniformly immune-depleted. Cytotoxic features were present in the non-neoplastic mucosa adjacent to the tumor in most MSS tumors, and intratumoral cytotoxic activation was observed in a subset.

Figure 5

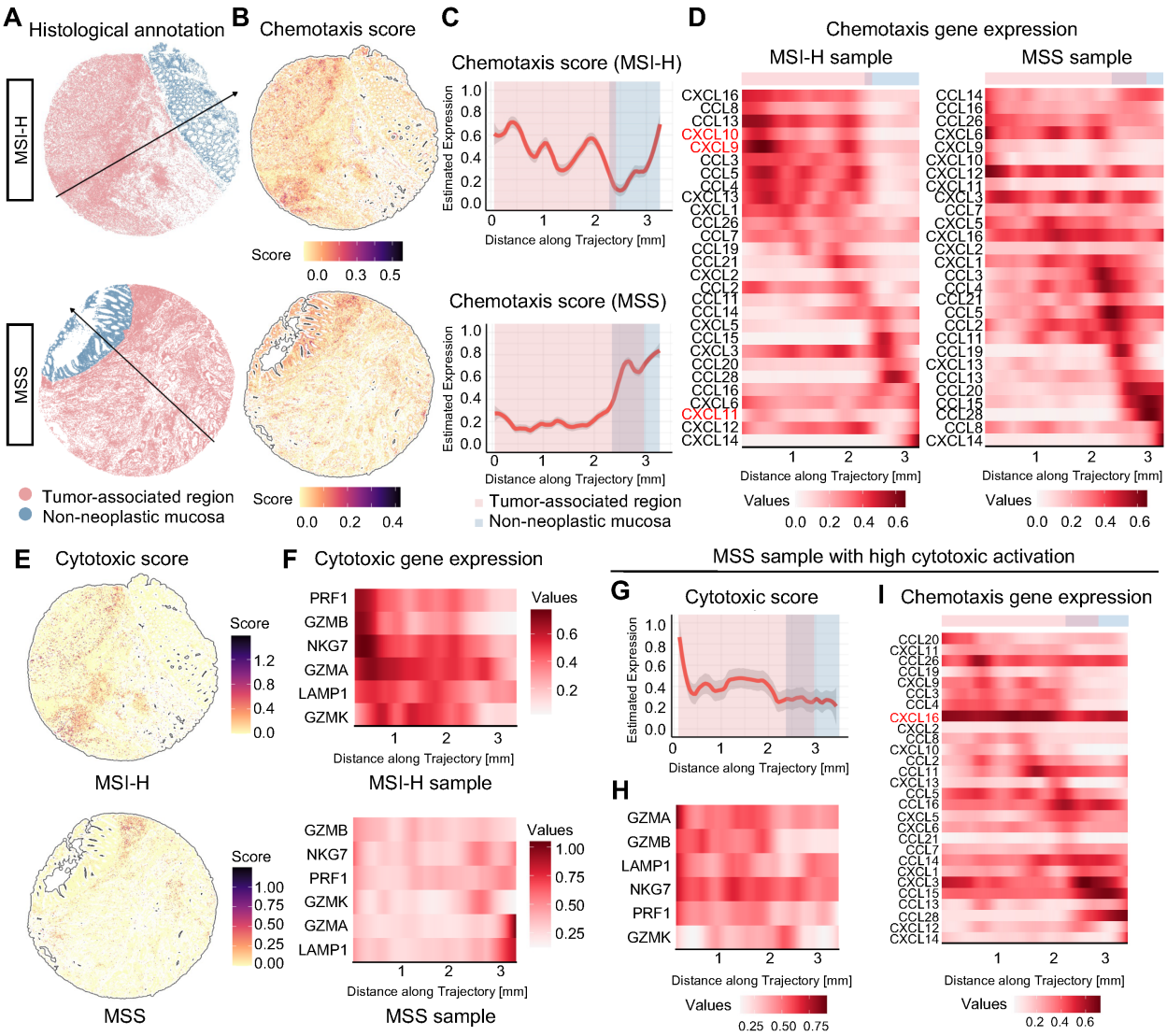

Figure 5. Spatial trajectory analysis

A, Surface plots displaying histological annotations for representative MSI-H (top) and MSS (bottom) samples. **B**, Surface plots displaying the distribution of chemotaxis scores in representative MSI-H (top) and MSS (bottom) samples. **C**, Line plots illustrating changes in

chemotaxis scores along spatial trajectories for representative MSI-H and MSS samples, estimated using SPATA2. Error bands represent 95% confidence intervals. **D**, Heatmap showing the expression of genes included in the chemotaxis score along the spatial trajectory for representative MSI-H and MSS samples. **E**, Surface plots showing the spatial distribution of cytotoxic scores in representative MSI-H (top) and MSS (bottom) samples. **F**, Heatmap showing the expression of genes included in the cytotoxic score along the spatial trajectory for representative MSI-H (top) and MSS (bottom) samples. **G**, Line plot illustrating changes in cytotoxic scores along spatial trajectory for an MSS sample with high cytotoxic activation. **H**, Heatmap showing the expression of genes included in the cytotoxic score along the spatial trajectory for the MSS sample shown in G. **I**, Heatmap showing the expression of genes included in the chemotaxis score along the spatial trajectory for the MSS sample shown in G.

Cellular neighborhood analysis reveals distinct multicellular architectures across tumor regions and microsatellite subtypes

To determine whether the spatially resolved cell states identified above were organized into higher-order tissue structures, we performed cellular neighborhood (CN) analysis using the cellular composition within a radius of 18.85 μm around each cell (Figure 6A). CN analysis identified recurrent multicellular niches spanning tumor-dominant, immune-enriched, stromal-enriched, and immune–stromal mixed states, including immune-mixed, tertiary lymphoid structures (TLS)-like, tumor–CD8 T cell, IgG^+ plasma, neutrophil, cancer-associated fibroblast (CAF), endothelial, and $CXCL14^+$ fibroblast–plasma niches.

Differential abundance analysis revealed marked differences in CN composition according to microsatellite status across both interface and tumor core regions. At the interface, MSI-H tumors were enriched for immune-associated neighborhoods, including tumor–CD8 T cell, neutrophil,

and IgG$^+$ plasma niches, whereas MSS tumors showed preferential enrichment of stromal-associated neighborhoods, including CXCL14$^+$ fibroblast–plasma and CAF niches, together with endothelial niches (Figure 6B). Within tumor core regions, tumor–CD8 T cell and neutrophil niches were enriched in MSI-H tumors, whereas endothelial and immune–stromal mixed niches were enriched in MSS tumors (Figure 6C). The enrichment of these niches in the interface was preserved when the interface was restricted to the tumor-associated region (Figure S8B). Spatial mapping of representative neighborhoods further illustrated these patterns, with tumor–CD8 T cell niches broadly distributed throughout MSI-H tumors, whereas CAF niches were preferentially localized within MSS tumors (Figure 6D-E, Figure S8C-D). Together, these findings demonstrate region-specific multicellular organization according to microsatellite status, with immune-associated neighborhoods predominating in MSI-H tumors and stromal- and endothelial-associated neighborhoods predominating in MSS tumors.

Figure 6

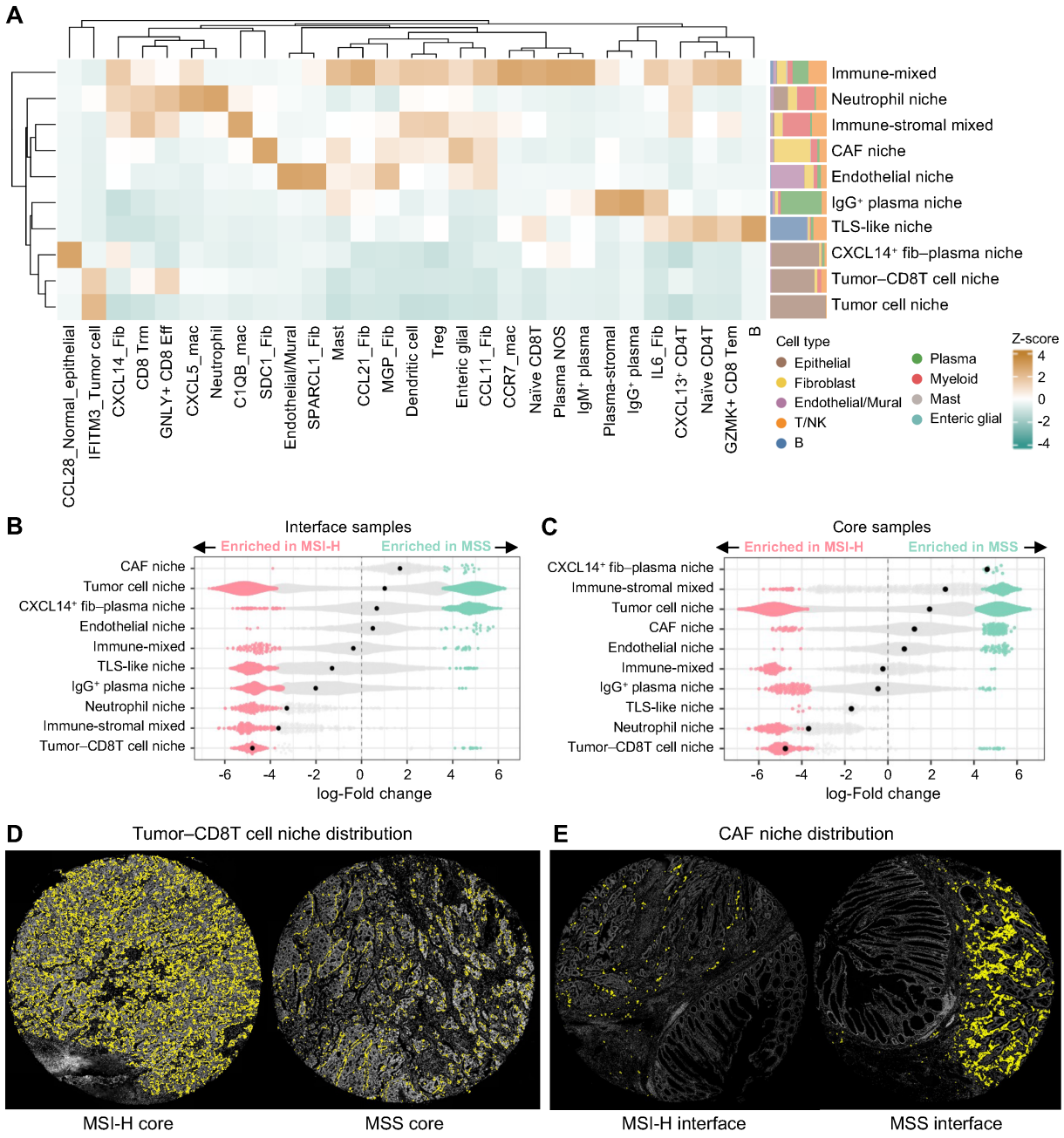

Figure 6. Cellular neighborhood architecture in MSI-H and MSS colorectal tumors

A, Heatmap showing the cellular composition of cellular neighborhoods (CNs), defined based on the cellular composition within a radius of 18.85 µm around each cell. **B,C**, Differential abundance analysis of CNs across MSI-H and MSS samples in the interface (B) and tumor core (C) using

Milo. Negative $\log_2$ fold changes indicate enrichment in MSI-H samples, and positive values indicate enrichment in MSS samples. **D,E**, Spatial distribution of representative CNs, including tumor–CD8 T cell and CAF niches.

Distinct multicellular niches are associated with local immune and stromal–vascular signaling programs

We next investigated whether these multicellular niches were associated with distinct local signaling programs. Using LIANA+ on Xenium data, we performed cell–cell interaction analysis within individual niches. Within the tumor–CD8 T cell niche, FASLG–FAS and IL15–IL2RB were among the top-ranked inferred interactions between $GNLY^+$ CD8 effector T cells and $IFITM3^+$ tumor cells (Figure 7A). Spatial visualization confirmed close proximity of these cell populations together with localized expression of the corresponding ligand and receptor transcripts (Figure 7B). To validate tumor-cell IL15 expression at the protein level, we performed dual immunofluorescence staining for IL15 and Pan-CK. Granular cytoplasmic IL15 staining was observed within $Pan\text{-}CK^+$ tumor cells (Figure 7C-D, Figure S9A), whereas the adjacent stromal compartment showed minimal signal, supporting tumor cells as a source of IL15. Among the predicted interactions, the IL15–IL2RB interaction was markedly enriched in MSI-H compared with MSS tumors, particularly within tumor–CD8 T cell niches (Figure 7E, Figure S9B). These findings indicate that immune-enriched niches in MSI-H tumors are associated with distinct local signaling programs involving cytotoxic lymphocyte–tumor cell interactions.

In contrast, cell–cell interaction analysis within the endothelial niche identified ligand–receptor interactions between fibroblasts and endothelial/mural cells, including VEGFA–FLT1 interactions (Figure 7F). Spatial mapping demonstrated close association between fibroblasts and endothelial cells, together with localized expression of VEGFA and FLT1 transcripts within interface regions

(Figure 7G). Quantitative analysis further revealed stronger inferred VEGFA–FLT1 interactions in MSS tumors, particularly within endothelial niches (Figure 7H, Figure S9C). These findings suggest that MSS-associated niches are characterized by inferred stromal–vascular interactions distinct from the immune effector interactions observed in MSI-H tumors.

Figure 7

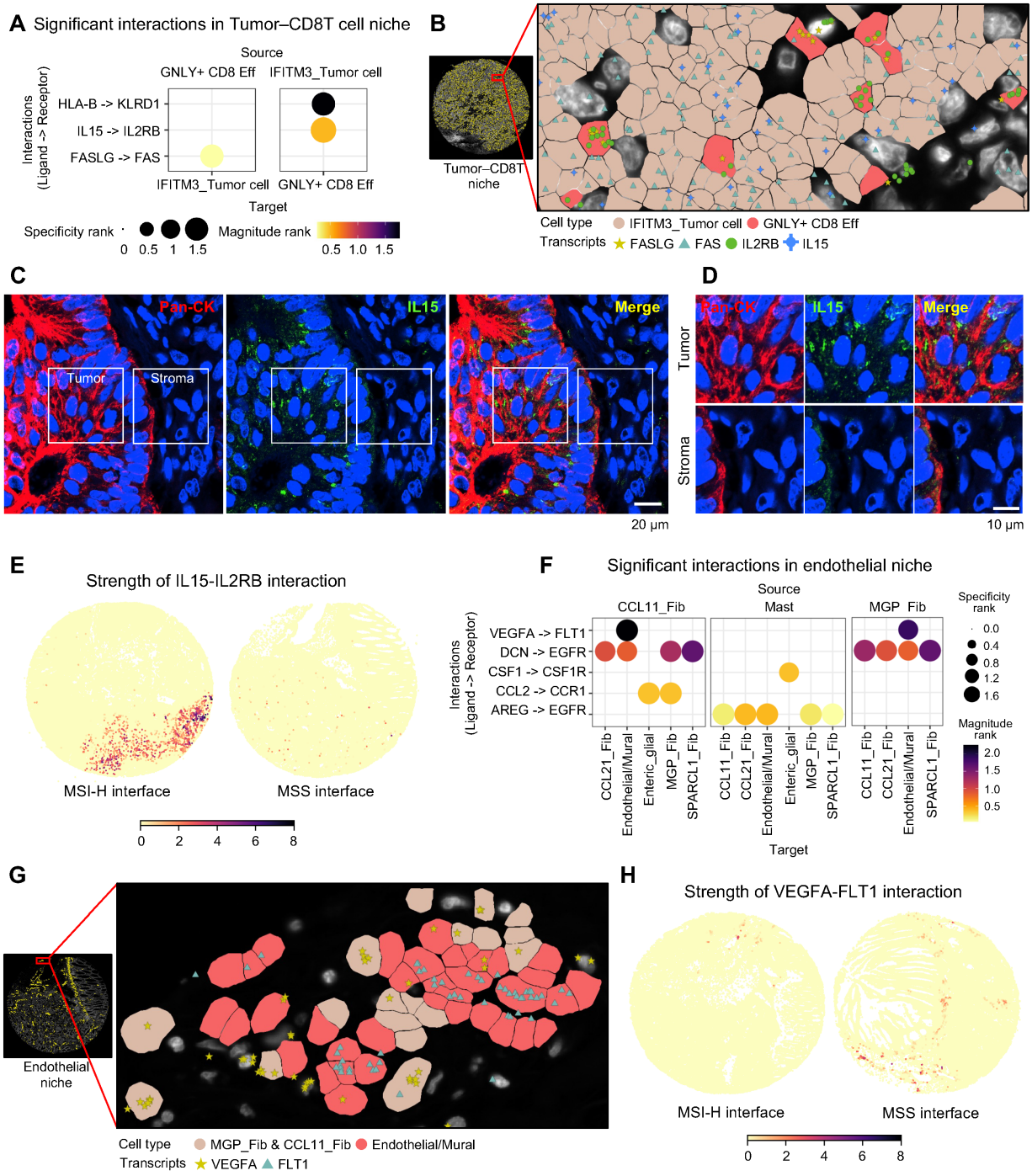

Figure 7. Ligand–receptor interactions within spatially defined cellular neighborhoods

A, Significant inferred ligand–receptor interactions identified within the tumor–CD8 T cell niche using LIANA+. **B**, Spatial visualization of the tumor–CD8 T cell niche showing interacting GNLY^{+}

CD8 effector T cells and IFITM3$^+$ tumor cells. **C**, Representative dual immunofluorescence images showing IL15 (green), Pan-CK (red), and DAPI (blue) in colorectal cancer tissue. **D**, Higher-magnification views of the boxed tumor and stromal regions in **C**, showing cytoplasmic IL15 staining in Pan-CK$^+$ tumor cells and minimal signal in the adjacent stroma. Scale bars, 20 μm (**C**) and 10 μm (**D**). **E**, Spatial mapping of inferred IL15–IL2RB interaction strength across MSI-H and MSS samples. **F**, Significant inferred ligand–receptor interactions identified within the endothelial niche. **G**, Spatial visualization of the endothelial niche highlighting stromal–vascular cell interactions. **H**, Spatial mapping of inferred VEGFA–FLT1 interaction strength across MSI-H and MSS samples.

Independent single-cell atlas supports immune and stromal programs identified by spatial transcriptomics

To determine whether the immune and stromal programs identified by spatial transcriptomics were also observed in an independent dataset, we analyzed a CRC scRNA-seq atlas comprising 104 MSI-H and 244 MSS cases [28]. Reclustering of the T/NK/ILC compartment resolved 12 lymphoid populations supported by canonical marker expression patterns (Figure S10A-B). Differential abundance analysis revealed marked differences in lymphoid-state composition between MSI-H and MSS samples (Figure S10C). MSS tumors were enriched for CD4T_Naive, CD4T_MAML2, and, to a lesser extent, CD4T_Th17, ILC, and Treg populations, whereas MSI-H tumors were enriched for proliferating T cells, CD8T_Trm, NK cells, CD8T_Naive, γδ T cells, and CD8T_Temra populations. These findings are consistent with the enrichment of cytotoxic and effector lymphoid populations observed in MSI-H tumors by Xenium analysis.

We next assessed whether myeloid programs identified by spatial analysis were similarly represented in the atlas. Differential abundance testing revealed significant enrichment of CXCL5$^+$

686 macrophages in MSI-H samples, whereas cDC2, cycling macrophages, and cDC1 populations
687 were preferentially enriched in MSS samples (Figure S10D). The enrichment of dendritic cell
688 populations in MSS tumors was consistent with our in-house Xenium data analysis.

689 Finally, cell–cell interaction analysis revealed that inferred IL15–IL2RB interactions were stronger
690 in MSI-H samples and VEGFA–FLT1 interactions were stronger in MSS samples (Figure S10E-
691 F). These findings are consistent with the inferred interactions identified by spatial transcriptomics.
692 In the Xenium data, these interactions were further localized to distinct spatial niches, including
693 tumor–CD8 T cell niches in MSI-H tumors and endothelial niches in MSS tumors, highlighting the
694 additional spatial context provided by Xenium analysis.

695

696 **Independent spatial transcriptomic dataset supports several key spatial patterns**

697 To assess whether key spatial findings were observed in an independent dataset, we analyzed a
698 publicly available Xenium dataset of colorectal cancer comprising one MSI and one MSS tumor,
699 each of which included the tumor core, the tumor–normal interface, the distal tumor region, and
700 the distal normal mucosa [29] (Figure 8A-B, Figure S12D). Cell types were annotated based on
701 canonical marker genes, identifying ten major cell types, nine myeloid subsets and five T cell
702 subsets (Figure 8A, Figure S11A-F). Consistent with our in-house data, B cells and plasma cells
703 were more abundant at the interface than in the tumor core, particularly in the MSI tumor, and
704 fibroblasts and endothelial cells were more abundant in the MSS tumor than in the MSI tumor in
705 both regions (Figure S11G). Comparisons of T cell and myeloid subtypes are shown in Figure
706 S11H and I, respectively.

707 We first examined trajectories across the interface, from the tumor-associated region to the non-
708 neoplastic mucosa (Figure 8C-F, Figure S12A). In the MSI tumor, cytotoxic and chemotaxis scores
709 were highest within the tumor-associated region, accompanied by CXCL9, CXCL10, and CXCL11

expression, and decreased toward the non-neoplastic mucosa (Figure 8D-F), consistent with the high cytotoxic activation and CXCL9/10/11 expression within the tumor-associated region in our cohort. In the MSS tumor, chemotaxis scores increased toward the non-neoplastic mucosa in both interface regions (Figure 8D, Figure S12A). A similar increase in the cytotoxic score was observed in MSS interface 1, consistent with our in-house findings (Figure 8E). To exclude the influence of non-neoplastic mucosa, we repeated the analysis within the tumor-associated region only, with trajectories running from its core-proximal edge to its mucosa-proximal edge, as in our in-house analysis (Figure S13A-E). In the MSS tumor, the chemotaxis score increased toward the mucosa-proximal edge of the tumor-associated region in both interface regions, accompanied by higher expression of CXCL12 (Figure S13B and E), consistent with our in-house observations. However, changes in the cytotoxic score along this trajectory were variable (Figure S13C).

We next examined trajectories from the distal tumor region to the malignant epithelial compartment of the interface (Figure 8G-J, Figure S12D). In the MSI tumor, cytotoxic and chemotaxis scores were highest in the distal tumor region, where GZMA and GZMB were predominantly expressed, and decreased toward the malignant epithelial compartment of the interface (Figure 8H and J, Figure S12E). Notably, however, CXCL9 and CXCL10 showed the opposite pattern in the MSI tumor, with higher expression in the malignant epithelial compartment of the interface than in the distal tumor region (Figure 8I). This observation complements our in-house finding that CXCL9, CXCL10, and CXCL11 were more highly expressed in the tumor-associated region of the interface than in the non-neoplastic mucosa in MSI-H tumors. In contrast, in the MSS tumor, both scores were low in the distal tumor region and higher in the malignant epithelial compartment of the interface (Figure 8H and J), in line with the higher T cell infiltration at the interface than in the tumor core observed in a subset of MSS tumors in our cohort. In both tumors, CXCL12 was more highly expressed within the malignant epithelial compartment of the interface (Figure 8I).

Finally, to assess whether mucosa-associated features at the interface reflected normal mucosal biology, we examined trajectories from the distal normal mucosa to the interface excluding the malignant epithelial compartment (Figure S12F-I). In both tumors, CCL15 and CCL28 were expressed in the distal normal mucosa and showed the highest relative expression around the junction between the distal normal mucosa and the non-neoplastic mucosa of the interface (Figure S12G-I). In addition, inferred IL15–IL2RB interactions between tumor cells and $CD8^+$ T cells were stronger in the MSI tumor than in the MSS tumor (Figure 8K). Although limited to one tumor per subtype, these results provide independent spatial support for several key patterns identified in our cohort.

Figure 8

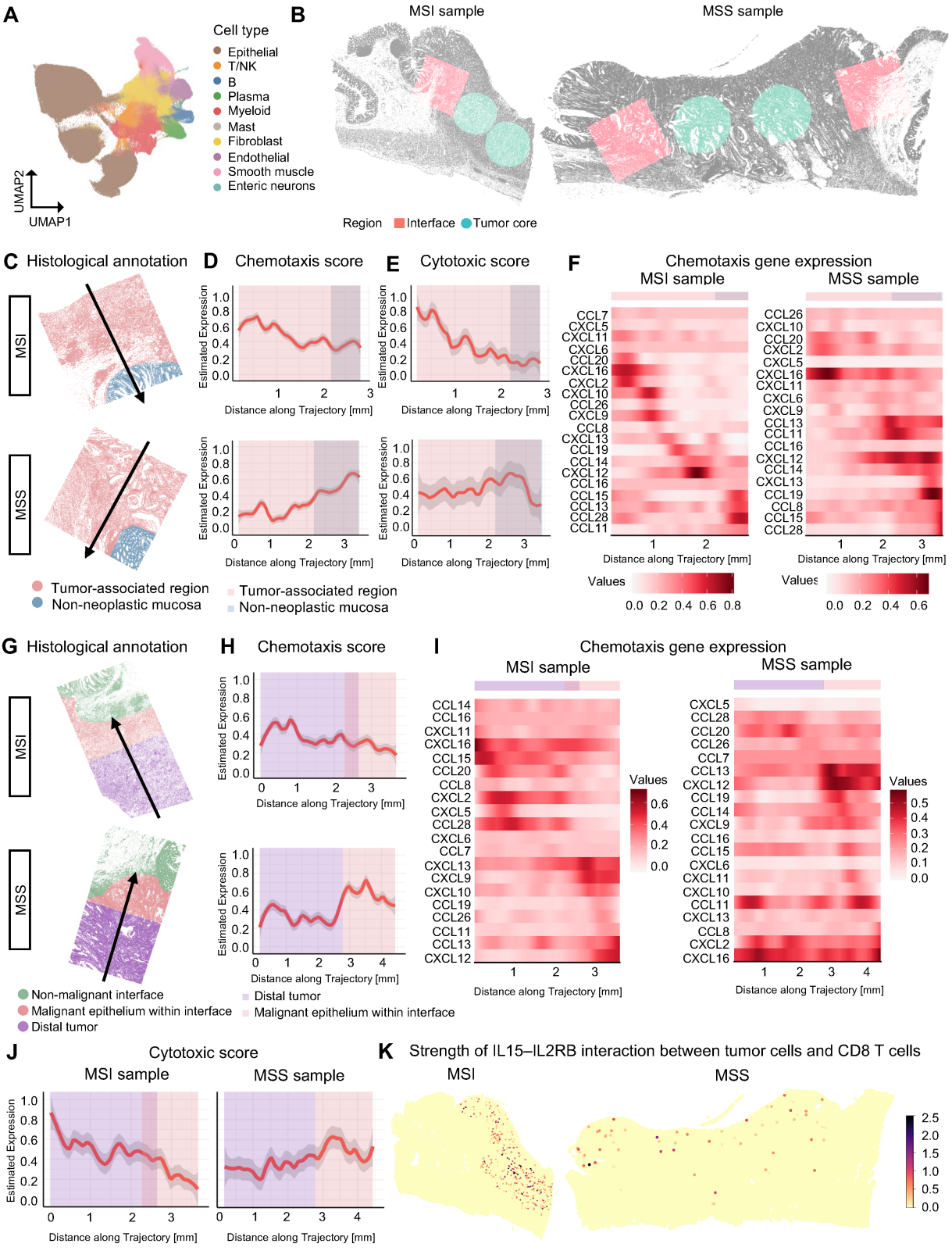
A
Cell type
Epithelial
T/NK
B
Plasma
Myeloid
Mast
Fibroblast
Endothelial
Smooth muscle
Enteric neurons
UMAP2
UMAP1
B
MSI sample
MSS sample
Region
Interface
Tumor core
C Histological annotation
MSI
MSS
Tumor-associated region
Non-neoplastic mucosa
D Chemotaxis score
E Cytotoxic score
Estimated Expression
Distance along Trajectory [mm]
F Chemotaxis gene expression
MSI sample
MSS sample
CCL7
CXCL5
CXCL11
CXCL6
CCL20
CXCL16
CXCL2
CXCL10
CCL26
CXCL9
CCL8
CXCL13
CCL19
CCL14
CXCL12
CCL16
CCL15
CCL13
CCL28
CCL11
CCL26
CXCL10
CCL20
CXCL2
CXCL5
CXCL16
CXCL11
CXCL6
CXCL9
CCL13
CCL11
CCL16
CXCL12
CCL14
CXCL13
CCL19
CCL8
CCL15
CCL28
Values
G Histological annotation
MSI
MSS
Non-malignant interface
Malignant epithelium within interface
Distal tumor
H Chemotaxis score
Distal tumor
Malignant epithelium within interface
I Chemotaxis gene expression
MSI sample
MSS sample
CCL14
CCL16
CXCL11
CXCL16
CCL15
CCL20
CCL8
CXCL2
CXCL5
CCL28
CXCL6
CCL7
CXCL13
CXCL9
CXCL10
CCL19
CCL26
CCL11
CCL13
CXCL12
CXCL5
CCL28
CCL20
CCL26
CCL7
CCL13
CXCL12
CCL19
CCL14
CXCL9
CCL16
CCL15
CXCL6
CXCL11
CXCL10
CCL11
CXCL13
CCL8
CXCL2
CXCL16
Values
J Cytotoxic score
MSI sample
MSS sample
Estimated Expression
Distance along Trajectory [mm]
K Strength of IL15–IL2RB interaction between tumor cells and CD8 T cells
MSI
MSS

744

Figure 8. Spatial trajectory and cell–cell interaction analyses using a publicly available colorectal cancer Xenium dataset

A, UMAP visualization of major cell types. **B**, Spatial maps showing the tumor–normal interface and tumor core regions in MSI and MSS samples. **C**, Histological annotations of the tumor-associated region and non-neoplastic mucosa in representative MSI and MSS samples. Black arrows indicate the direction of the spatial trajectories. **D, E**, Line plots illustrating changes in chemotaxis (D) and cytotoxic (E) scores along spatial trajectories for representative MSI and MSS samples. Error bands represent 95% confidence intervals. **F**, Heatmap showing the expression of genes included in the chemotaxis score along the spatial trajectory for representative MSI and MSS samples. **G**, Histological annotations of the distal tumor region and the malignant epithelial compartment of the interface in MSI and MSS samples. Black arrows indicate the direction of the spatial trajectories. **H**, Line plots illustrating changes in chemotaxis scores along spatial trajectories from the distal tumor region to the malignant epithelial compartment of the interface. **I**, Heatmap showing the expression of genes included in the chemotaxis score along the spatial trajectory. **J**, Line plots illustrating changes in cytotoxic scores along spatial trajectories. **K**, Spatial maps showing inferred IL15–IL2RB interactions between tumor cells and CD8 T cells in MSI and MSS samples.

Discussion

Our study shows that the lateral tumor–normal interface displays features contrasting with those reported at invasive fronts. The invasive front has traditionally been defined as the leading edge of tumor invasion and is characterized by accumulation of CAFs, myeloid cells, extracellular matrix remodeling, angiogenesis, and epithelial plasticity, all of which contribute to tumor budding, local invasion, and metastatic dissemination [3, 33]. Spatial and histopathologic studies have

consistently shown enrichment of stromal and myeloid populations at invasive fronts, where CAF-derived extracellular matrix programs and myeloid-mediated inflammatory signals cooperatively promote tumor progression [4, 34]. In contrast, our analysis of the lateral tumor–normal interface revealed relative depletion of both fibroblast and myeloid populations compared with tumor core regions. This suggests that the interface is not simply another representation of the invasive front, but may instead represent a distinct immune–stromal boundary encompassing both tumor and non-invaded normal compartments, although a direct comparison within the same tumors will be required to confirm this distinction. Analyzing this boundary may thereby capture biological processes that are not readily apparent from analyses focused on intratumoral regions.

A second notable feature of the tumor–normal interface was the preservation of a homeostatic mucosal immune program despite its immediate proximity to tumor tissue. B cells and plasma cells were consistently enriched at the interface irrespective of microsatellite status, suggesting retention of immune features normally associated with healthy colorectal mucosa. Importantly, this enrichment persisted after excluding non-neoplastic mucosa, indicating that it was also present within the tumor-associated region. Consistent with this observation, trajectory analysis identified preferential expression of CXCL12 and CXCL14 toward the non-neoplastic mucosa even within the tumor-associated region. CXCL14 has been implicated in immune surveillance through recruitment of dendritic cells, NK cells, and other immune populations to peripheral tissues [35, 36], while frequently being downregulated during colorectal tumorigenesis [37]. Together, these findings suggest that the interface partly retains immune programs normally associated with healthy colorectal mucosa, even within the tumor-associated region.

A key finding of our study is that MSS colorectal cancers are not uniformly immune-cold. Although MSS tumor cores frequently displayed features consistent with immune exclusion, including enrichment of regulatory T cell populations and diminished cytotoxic T cell activity [38], immune activity was present at the tumor–normal interface in a subset of MSS tumors. Indeed, several

MSS tumors exhibited immune-enriched or immune-intermediate interfaces despite immune-depleted tumor cores. Within MSS tumors, naïve $CD4^+$ T cells were also preferentially localized to the interface.

In contrast, MSI-H tumors maintained immune activation across both interface and tumor core, accompanied by enrichment of CD8 Trm cells, $GNLY^+$ effector T cells, and immune-associated cellular neighborhoods. MSI-H tumors expressed CXCL9, CXCL10, and CXCL11, chemokines known to recruit cytotoxic T cells, NK cells, and Th1 lymphocytes [31], at higher levels within the tumor-associated region than in the non-neoplastic mucosa. Notably, in the independent spatial dataset, CXCL9 and CXCL10 were more highly expressed at the interface than in the distal tumor region of the MSI tumor, despite higher overall cytotoxic activation in the distal tumor region. This raises the possibility that CXCR3-ligand expression is a characteristic feature of the MSI-H interface. Activation of STING signaling has been shown to induce these chemokines and promote antitumor immune recruitment in colorectal cancer [39], suggesting a potential mechanism underlying this pattern. However, because this observation was based on a single MSI tumor and our in-house samples did not include a continuous region spanning the tumor core and the interface, this possibility requires validation in larger cohorts.

In MSS tumors, cytotoxic scores increased toward the non-neoplastic mucosa, but this increase was no longer observed when the analysis was restricted to the tumor-associated region, whereas chemotaxis scores continued to increase toward its mucosa-proximal edge. A similar pattern was observed in the MSS tumor of the independent spatial dataset, in which the chemotaxis score increased toward the mucosa-proximal edge, whereas changes in the cytotoxic score were variable. Together, these observations suggest that differences between MSI-H and MSS tumors may involve not only immune-cell abundance but also the spatial relationship between chemotactic and cytotoxic features. The relationship between these spatial patterns and immune infiltration into the tumor core remains to be determined.

Cellular neighborhood analysis further showed that differences in immune organization between MSI-H and MSS tumors were associated with discrete multicellular niches. Within tumor–CD8 T cell niches, IL15–IL2RB emerged as a strong inferred interaction between tumor cells and GNLY^{+} CD8 effector T cells, whereas endothelial niches in MSS tumors were characterized by a strong inferred VEGFA–FLT1 interaction between stromal and vascular cells. Dual immunofluorescence supported IL15 protein expression in Pan-CK^{+} tumor cells. Previous studies have linked IL15 deletion and reduced expression to increased recurrence risk in colorectal cancer [40], while higher densities of IL2RB^{+} cytotoxic T cells have been associated with favorable clinical outcomes in esophageal squamous cell carcinoma [41]. These findings suggest that distinct interface niches are associated with different biological states, with inferred IL15–IL2RB interactions potentially related to local cytotoxic immune activation and VEGFA–FLT1 interactions to stromal–vascular organization.

However, several alternative explanations should be considered. The lower immune activity in MSS tumor cores may reflect tumor-intrinsic mechanisms of immune exclusion, such as reduced neoantigen load, antigen loss, or downregulation of MHC class I, as well as stromal barriers formed by cancer-associated fibroblasts, rather than restriction of immune cell entry at the interface. Because our panel included only a limited number of genes related to antigen presentation and TGF-β signaling, these mechanisms could not be directly assessed in this study. Functional studies will be required to determine whether the spatial patterns identified at the interface causally influence immune infiltration into the tumor core.

This study has several limitations. First, the spatial cohort was small. The patient-level checks assessed directional consistency and sensitivity to the exclusion of individual patients; they did not establish that statistical significance persists after patient exclusion, and several MSI-H–MSS differences were possibly driven by individual patients (Table S3). These findings should therefore be considered exploratory. Second, the targeted panel lacked several stromal, MHC class I and

immunoglobulin heavy-chain genes. Third, the independent spatial dataset included only one tumor per subtype. Fourth, the CN analysis excluded sparsely populated windows, and spatial gradients may partly reflect differences in cell composition. Finally, this observational study cannot establish causality, and LIANA+ infers ligand–receptor interactions from co-expression rather than demonstrating signal transduction.

Conclusions

In conclusion, our spatial transcriptomic analysis identifies the tumor–normal interface as a previously underappreciated compartment of colorectal cancer that differs from the tumor core and shows features contrasting with those reported at invasive fronts. Irrespective of microsatellite status, the interface shared common features, including the enrichment of B cells and plasma cells relative to the tumor core and increasing CXCL14 expression toward the non-neoplastic mucosa in most tumors. At the same time, the interface was where differences in immune organization between MSI-H and MSS tumors were most evident, including IFN-γ–associated chemokine expression, cytolytic activity and multicellular niches. Notably, MSS colorectal cancers were not uniformly immune-cold, with a subset retaining higher T cell density at the interface than in the tumor core.

Together, these results highlight the importance of incorporating spatial context when investigating antitumor immunity in colorectal cancer. Our findings may provide a rationale for exploring therapeutic strategies aimed at remodeling interface-associated immune programs in MSS colorectal cancer. However, because this study is observational and based on a small cohort, these findings should be regarded as hypothesis-generating and warrant functional validation in larger cohorts.

Abbreviations

CRC: Colorectal cancer; EMT: Epithelial–mesenchymal transition; MSI-H: Microsatellite instability-high; MSI-L: Microsatellite instability-low; MSS: Microsatellite stable; scRNA-seq: Single-cell RNA sequencing; FFPE: Formalin-fixed paraffin-embedded; PNA: Peptide nucleic acid; PCA: Principal component analysis; UMAP: Uniform Manifold Approximation and Projection; KNN: K-nearest neighbor; FDR: False discovery rate; CI: Confidence interval; NOS: Not otherwise specified; GO: Gene Ontology; LOESS: Locally estimated scatterplot smoothing; CN: Cellular neighborhood; L–R: Ligand–receptor; Treg: Regulatory T cells; CD8 Trm: Tissue-resident memory CD8 T cells; $GZMK^+$ CD8 Tem: $GZMK^+$ CD8 effector memory T cells; TLS: Tertiary lymphoid structures; CAF: Cancer-associated fibroblast; STING: Stimulator of interferon genes; R: Responder; NR: Non-responder

Data Availability

The Xenium data generated in this study have been deposited in the Gene Expression Omnibus under accession number GSE352247. The scRNA-seq data analyzed in this study were obtained from the CRC atlas project website (https://crc.icbi.at/) and the public Xenium dataset was obtained from the DDBJ Genomic Expression Archive (accession number E-GEAD-1117). The analysis scripts used in this study are available on Zenodo (https://doi.org/10.5281/zenodo.23849883).

Acknowledgements

S.B.L. is supported by the Korea Health Technology R&D Project through the Korea Health Industry Development Institute (KHIDI), funded by the Ministry of Health & Welfare, Republic of Korea (HR22C1734 and RS-2025-02310331), the National Research Foundation (NRF) of Korea (RS-2020-NR049588, RS-2020-NR046270, 2022R1C1C1004756), and the Korea-US Collaborative Cancer R&D Program funded by the Ministry of Health & Welfare, Republic of Korea (RS-2025-02223036). D.L. is supported by the National Research Foundation (NRF) of Korea

(RS-2025-00516273, RS-2025-19663014, RS-2026-25518552). FigureLabs was used to assist with the preparation of the study-design schematic overview in Figure 1A.

Author Contributions

D.L. and S.B.L. were responsible for the overall study design, coordination of the research, and establishment of the research objectives. J.K. and D.L. collected tissue samples and clinical data. D.L. performed pathology review and annotation. A.U. contributed to the overall bioinformatics analysis. D.L. and A.U. wrote the manuscript, with all authors contributing to its review and editing. All authors reviewed and approved the manuscript.

Competing interests

The authors declare no competing interests.

References

1. Zlobec I, Lugli A. Invasive front of colorectal cancer: dynamic interface of pro-/anti-tumor factors. World J Gastroenterol. 2009; 15: 5898-906.
2. Lugli A, Karamitopoulou E, Zlobec I. Tumour budding: a promising parameter in colorectal cancer. Br J Cancer. 2012; 106: 1713-7.
3. Alver TN, Bergholtz H, Holm MB, Dorg LT, Skrede ML, Kure EH, et al. Spatial Transcriptomics Reveals Cancer and Stromal Cell Heterogeneity Between Center and Invasive Front of Pancreatic Cancer. Mod Pathol. 2025; 38: 100726.
4. Li S, Xu F, Zhang J, Wang L, Zheng Y, Wu X, et al. Tumor-associated macrophages remodeling EMT and predicting survival in colorectal carcinoma. OncoImmunology. 2018; 7: e1380765.
5. Brisam M, Rauthe S, Hartmann S, Linz C, Brands RC, Kubler AC, et al. Expression of MAGE-A1-A12 subgroups in the invasive tumor front and tumor center in oral squamous cell carcinoma. Oncol Rep. 2016; 35: 1979-86.
6. Peterson LW, Artis D. Intestinal epithelial cells: regulators of barrier function and immune homeostasis. Nat Rev Immunol. 2014; 14: 141-53.
7. Hunter MV, Moncada R, Weiss JM, Yanai I, White RM. Spatially resolved transcriptomics reveals the architecture of the tumor-microenvironment interface. Nat Commun. 2021; 12: 6278.
8. Li R, Ferdinand JR, Loudon KW, Bowyer GS, Laidlaw S, Muyas F, et al. Mapping single-cell transcriptomes in the intra-tumoral and associated territories of kidney cancer. Cancer Cell. 2022; 40: 1583-99.e10.
9. Stahl PL, Salmen F, Vickovic S, Lundmark A, Navarro JF, Magnusson J, et al. Visualization and analysis of gene expression in tissue sections by spatial transcriptomics. Science. 2016; 353: 78-82.
10. Pelka K, Hofree M, Chen JH, Sarkizova S, Pirl JD, Jorgji V, et al. Spatially organized multicellular immune hubs in human colorectal cancer. Cell. 2021; 184: 4734-52 e20.
11. Hao Y, Stuart T, Kowalski MH, Choudhary S, Hoffman P, Hartman A, et al. Dictionary learning for integrative, multimodal and scalable single-cell analysis. Nat Biotechnol. 2024; 42: 293-304.

12. Dann E, Henderson NC, Teichmann SA, Morgan MD, Marioni JC. Differential abundance testing on single-cell data using k-nearest neighbor graphs. Nat Biotechnol. 2022; 40: 245-53.
13. Gombin J, Vaidyanathan R, Agafonkin V. [Internet] concaveman: A Very Fast 2D Concave Hull Algorithm. R package version 1.2.0. 2025. https://joelgombin.github.io/concaveman/.
14. Pebesma E. Simple Features for R: Standardized Support for Spatial Vector Data. R J. 2018; 10/1: 439-46.
15. Pagès F, Mlecnik B, Marliot F, Bindea G, Ou F-S, Bifulco C, et al. International validation of the consensus Immunoscore for the classification of colon cancer: a prognostic and accuracy study. Lancet. 2018; 391: 2128-39.
16. Guo G, Wang Y, Zhou Y, Quan Q, Zhang Y, Wang H, et al. Immune cell concentrations among the primary tumor microenvironment in colorectal cancer patients predicted by clinicopathologic characteristics and blood indexes. J Immunother Cancer. 2019; 7: 179.
17. Lea D, Watson M, Skaland I, Hagland HR, Lillesand M, Gudlaugsson E, et al. A template to quantify the location and density of CD3 + and CD8 + tumor-infiltrating lymphocytes in colon cancer by digital pathology on whole slides for an objective, standardized immune score assessment. Cancer Immunol Immunother. 2021; 70: 2049-57.
18. Marliot F, Chen X, Kirilovsky A, Sbarrato T, El Sissy C, Batista L, et al. Analytical validation of the Immunoscore and its associated prognostic value in patients with colon cancer. J Immunother Cancer. 2020; 8: e000272.
19. Gonzalez-Kozlova E, Sweeney R, Figueiredo I, Tuballes K, Ozbey S, Hamon P, et al. Humoral IgG1 responses to tumor antigens underpin clinical outcomes in immune checkpoint blockade. Nat Med. 2026; 32: 978-91.
20. Kueckelhaus J, Frerich S, Kada-Benotmane J, Koupourtidou C, Ninkovic J, Dichgans M, et al. Inferring histology-associated gene expression gradients in spatial transcriptomic studies. Nat Commun. 2024; 15: 7280.
21. Ashburner M, Ball CA, Blake JA, Botstein D, Butler H, Cherry JM, et al. Gene Ontology: tool for the unification of biology. Nat Genet. 2000; 25: 25-9.
22. Qiu X, Zhou T, Li S, Wu J, Tang J, Ma G, et al. Spatial single-cell protein landscape reveals vimentin-high macrophages as immune-suppressive in the microenvironment of hepatocellular carcinoma. Nat Cancer. 2024; 5: 1557-78.
23. Dimitrov D, Schäfer PSL, Farr E, Rodriguez-Mier P, Lobentanzer S, Badia-i-Mompel P, et al. LIANA+ provides an all-in-one framework for cell–cell communication inference. Nat Cell Biol. 2024; 26: 1613-22.
24. Efremova M, Vento-Tormo M, Teichmann SA, Vento-Tormo R. CellPhoneDB: inferring cell–cell communication from combined expression of multi-subunit ligand–receptor complexes. Nat Protoc. 2020; 15: 1484-506.
25. Jin S, Guerrero-Juarez CF, Zhang L, Chang I, Ramos R, Kuan C-H, et al. Inference and analysis of cell-cell communication using CellChat. Nat Commun. 2021; 12: 1088.
26. Hou R, Denisenko E, Ong HT, Ramilowski JA, Forrest ARR. Predicting cell-to-cell communication networks using NATMI. Nat Commun. 2020; 11: 5011.
27. Cabello-Aguilar S, Alame M, Kon-Sun-Tack F, Fau C, Lacroix M, Colinge J. SingleCellSignalR: inference of intercellular networks from single-cell transcriptomics. Nucleic Acids Res. 2020; 48: e55.
28. Marteau V, Nemati N, Handler K, Raju D, Kirchmair A, Rieder D, et al. Single-cell integration and multi-modal profiling reveals phenotypes and spatial organization of neutrophils in colorectal cancer. Cancer Cell. 2026; 44: 146-65.e14.
29. Iwane K, Nakanishi Y, Muta Y, Chen J, Yasumura K, Omatsu M, et al. Targeting fibroblast derived thrombospondin 2 disrupts an immune-exclusionary environment at the tumor front in colorectal cancer. Nat Commun. 2025; 16: 11590.
30. Mlecnik B, Bindea G, Angell HK, Maby P, Angelova M, Tougeron D, et al. Integrative Analyses of Colorectal Cancer Show Immunoscore Is a Stronger Predictor of Patient Survival Than Microsatellite Instability. Immunity. 2016; 44: 698-711.
31. Groom JR, Luster AD. CXCR3 ligands: redundant, collaborative and antagonistic functions. Immunol Cell Biol. 2011; 89: 207-15.
32. Di Pilato M, Kfuri-Rubens R, Pruessmann JN, Ozga AJ, Messemaker M, Cadilha BL, et al. CXCR6 positions cytotoxic T cells to receive critical survival signals in the tumor microenvironment. Cell. 2021; 184: 4512-30.e22.
33. García-Rodríguez JL, Korsgaard U, Vissing SM, Paasch TP, Semenova M, Vendelbo SL, et al. Cancer-associated fibroblasts shape the formation of budding cancer cells at the invasive front of human colorectal cancer. Commun Biol. 2025; 8: 1345.
34. Quail DF, Joyce JA. Microenvironmental regulation of tumor progression and metastasis. Nat Med. 2013; 19: 1423-37.

35. Shellenberger TD, Wang M, Gujrati M, Jayakumar A, Strieter RM, Burdick MD, et al. BRAK/CXCL14 is a potent inhibitor of angiogenesis and a chemotactic factor for immature dendritic cells. Cancer Res. 2004; 64: 8262-70.
36. Westrich JA, Vermeer DW, Silva A, Bonney S, Berger JN, Cicchini L, et al. CXCL14 suppresses human papillomavirus-associated head and neck cancer through antigen-specific CD8(+) T-cell responses by upregulating MHC-I expression. Oncogene. 2019; 38: 7166-80.
37. Cao B, Yang Y, Pan Y, Jia Y, Brock MV, Herman JG, et al. Epigenetic silencing of CXCL14 induced colorectal cancer migration and invasion. Discov Med. 2013; 16: 137-47.
38. Llosa NJ, Cruise M, Tam A, Wicks EC, Hechenbleikner EM, Taube JM, et al. The vigorous immune microenvironment of microsatellite instable colon cancer is balanced by multiple counter-inhibitory checkpoints. Cancer Discov. 2015; 5: 43-51.
39. Vornholz L, Isay SE, Kurgyis Z, Strobl DC, Loll P, Mosa MH, et al. Synthetic enforcement of STING signaling in cancer cells appropriates the immune microenvironment for checkpoint inhibitor therapy. Sci Adv. 2023; 9: eadd8564.
40. Mlecnik B, Bindea G, Angell HK, Sasso MS, Obenauf AC, Fredriksen T, et al. Functional Network Pipeline Reveals Genetic Determinants Associated with in Situ Lymphocyte Proliferation and Survival of Cancer Patients. Sci Transl Med. 2014; 6: 228ra37.
41. You Y, Gao L, Li S, Huang H, Wang T, Nie Z, et al. IL-15 signaling via cis- and trans-presentation to progenitor-exhausted CD8+ T cells enhances radio-immunotherapy efficacy in ESCC. J Nanobiotechnology. 2026; 24: 13.